Skin inflammation driven by differentiation of quiescent tissue-resident ILCs into a spectrum of pathogenic effectors

Piotr Bielecki*[,1], Samantha J. Riesenfeld*[,2], Monika S. Kowalczyk*[,2], Maria C. Amezcua Vesely[1,3], Lina Kroehling[1], Parastou Yaghoubi[1], Danielle Dionne[2], Abigail Jarret[1], Holly R. Steach[1], Heather M. McGee[1,4], Caroline B. M. Porter[2], Paula Licona-Limon[1,5], Will Bailis[1], Ruaidhri P. Jackson[1], Nicola Gagliani[1,6,7,8], Richard M. Locksley[3,9] Aviv Regev[^,2,3,10], Richard A. Flavell[^1,3]

[*]These co-first authors contributed equally to this work

[1]Department of Immunobiology, Yale University School of Medicine, New Haven, CT 06520, USA

[2]Klarman Cell Observatory, Broad Institute of MIT and Harvard, Cambridge MA 02142

[3]Howard Hughes Medical Institute

[4] Department of Radiation Oncology, Icahn School of Medicine at Mount Sinai, New York, NY 10029

[5]Departamento de Biología Celular y del Desarrollo, Instituto de Fisiología Celular, Universidad Nacional Autónoma de México, México City 04510

[6]Department of General, Visceral and Thoracic Surgery, University Medical Center Hamburg-Eppendorf, 20246 Hamburg, Germany;

[7]I. Department of Medicine, University Medical Center Hamburg-Eppendorf Hamburg-Eppendorf, 20246 Hamburg, Germany;

[8]Immunology and Allergy Unit, Department of Medicine Solna, Karolinska Institute, 17176 Stockholm, Sweden

[9]Department of Medicine, University of California San Francisco, San Francisco, CA, USA

[10]Koch Institute of Integrative Cancer Research, Department of Biology, Massachusetts Institute of Technology, Cambridge, MA 02140

^Correspondence to: A.R aregev@broadinstitute.com and R.A.F richard.flavell@yale.edu

Psoriasis pathology is driven by the type 3 cytokines IL-17 and Il-22, but little is understood about the dynamics that initiate alterations in tissue homeostasis. Here, we use mouse models, single-cell RNA-seq (scRNA-seq), computational inference and cell lineage mapping to show that psoriasis induction reconfigures the functionality of skin-resident ILCs to initiate disease. Tissue-resident ILCs amplified an initial IL-23 trigger and were sufficient, without circulatory ILCs, to drive pathology, indicating that ILC tissue remodeling initiates psoriasis. Skin ILCs expressed type 2 cytokines IL-5 and IL-13 in steady state, but were epigenetically poised to become ILC3-like cells. ScRNA-seq profiles of ILCs from psoriatic and naïve skin of wild type (WT) and *Rag1*$^{-/-}$ mice form a dense continuum, consistent with this model of fluid ILC states. We inferred biological "topics" underlying these states and their relative importance in each cell with a generative model of latent Dirichlet allocation, showing that ILCs from untreated skin span a spectrum of states, including a naïve/quiescent-like state and one expressing the *Cd74* and *Il13* but little *Il5*. Upon disease induction, this spectrum shifts, giving rise to a greater proportion of classical *Il5*- and *Il13*-expressing "ILC2s" and a new, mixed ILC2/ILC3-like subset, expressing *Il13, Il17,* and *Il22*. Using these key topics, we related the cells through transitions, revealing a quiescence-ILC2-ILC3s state trajectory. We demonstrated this plasticity *in vivo*, combining an IL-5 fate mouse with IL-17A and IL-22 reporters, validating the transition of IL-5–producing ILC2s to IL-22– and IL-17A–producing cells during disease initiation. Thus, steady-state skin ILCs are actively repressed and cued for a plastic, type 2 response, which, upon induction, morphs into a type 3 response that drives psoriasis. This suggests a general model where specific immune activities are primed in healthy tissue, dynamically adapt to provocations, and left unchecked, drive pathological remodeling.

49 **INTRODUCTION**

50 Psoriasis pathology is driven by the type 3 cytokines IL-17 and Il-22 (Nograles, Zaba et al. 2008,
51 Cai, Shen et al. 2011). The dermal inflammation and acanthosis induced by IL-23 are thought to
52 be mediated by the Th17-cell associated cytokine IL-22. While both IL-17 and IL-22 are produced
53 at elevated levels in psoriatic skin, the major cell source of these cytokines during disease remains
54 unclear. In psoriasis patients, γδ T cells were found to be greatly increased in affected skin and
55 produced large amounts of IL-17, suggesting they may play a key role in pathogenesis (Cai, Shen
56 et al. 2011). Recently, however, IL-17 and IL-22 producing ILC3s have been proposed to be a
57 significant source of cytokine production during psoriasis (Teunissen, Munneke et al. 2014,
58 Villanova, Flutter et al. 2014). These cells are thought to be activated in response to IL-1β and IL-
59 23, whose levels correlate with disease severity, and are decreased following antitumor necrosis
60 factor-α (anti-TNFα) treatment. The presence of a novel ILC population in psoriatic skin that
61 responds to one of the most effective biologic therapeutics suggests that dysregulation of ILCs is
62 a contributing factor to psoriasis pathogenesis. While ILC3s dominate psoriatic skin (Pantelyushin,
63 Haak et al. 2012), in healthy individuals the majority of ILCs are represented by group 2 ILCs,
64 defined by IL-5 and IL-13 production (Roediger, Kyle et al. 2013, Spencer, Wilhelm et al. 2014).
65 We wanted to determine at what point during disease progression the frequency of ILC2s and
66 ILC3s shifts and whether a potential for conversion between these cell types underlies this disease.
67

68 High parallel single-cell RNA sequencing (scRNA-seq) has become a powerful tool for unbiased
69 analysis of various cells types. Analyses of immune cell classes, such as ILCs, typically treat them
70 as collections of discrete immune cell "types", yet these cell types may share important biological
71 signals and have been observed in some contexts to essentially continuously span a functional

spectrum. To capture and explore fluid, mixed transcriptional states, we used latent Dirichlet allocation (LDA), or "topic modeling", a statistical data mining approach for discovering the abstract topics that explain the words occurring in a collection of text documents (Blei 2003). Applied to scRNA-Seq, each "document" corresponds to a cell, and a "topic" corresponds to a biological program, modeled as a distribution over expressed genes, rather than words. Given the number of topics as a parameter, both topics and the mixture weights in cells are inferred without supervision. LDA was independently introduced in population genetics to model admixed individuals with ancestry from multiple populations (Pritchard, Stephens et al. 2000). In genomics, it has been applied to deconvolute cell types in population RNA-seq (Repsilber, Kern et al. 2010, Schwartz and Shackney 2010, Shen-Orr, Tibshirani et al. 2010, Ahn, Yuan et al. 2013, Lindsay 2013, Quon, Haider et al. 2013, Wang, Gong et al. 2015), and proposed for finding structure in bulk or single-cell RNA-seq, for example, in inference of confounding batch effects (Dey, Hsiao et al. 2017).

RESULTS

To determine which cells are key to initiate psoriatic disease, we studied a subcutaneous IL-23 injection model, which leads to increased skin thickness after five days of daily injections (**Fig. 1A**, **Fig. S1A**). First, we assessed the role of different immune cell types in this model (**Fig. 1B**, **Fig. S1B and C**). Consistent with previous results, the *Rag2*$^{-/-}$ *Il2rg*$^{-/-}$ double mutant, which lacks all lymphocytes, did not show any increase in ear thickness, whereas *Rag1*$^{-/-}$ mice, which have intact ILCs, showed significant increase in skin thickness over the treatment course. This is also consistent with an increased number of human ILC3s recently observed in psoriatic patients (Teunissen, Munneke et al. 2014, Villanova, Flutter et al. 2014). Moreover, while γδ T cells have

been implicated in a longer treatment course (Cai, Shen et al. 2011, Pantelyushin, Haak et al. 2012), analyzing *Tcrd*$^{-/-}$ mice, which lack only γδ T cells, we found no evidence that they contribute to disease initiation (**Fig. 1B**). Next, to further confirm the role of ILCs in disease initiation, we adoptively transferred sorted skin ILCs from untreated WT mice into *Rag2*$^{-/-}$ *Il2rg*$^{-/-}$ mice, and observed significant skin thickening in treated versus untreated recipient mice (**Fig. 1C**). Finally, we assessed the contributions of circulatory versus tissue-resident lymphocytes in the psoriasis model, because recent studies of inflammation in several peripheral tissues suggested different involvement of circulatory and tissue resisdent ILCs (Dyring-Andersen, Geisler et al. 2014, Gasteiger, Fan et al. 2015, Li, Hodgkinson et al. 2016, Yang, Hu et al. 2016, Huang, Mao et al. 2018). We compared disease phenotype between control mice and those treated with FTY720, which blocks signaling from the S1P1 receptor, preventing egress of T cells from secondary lymphoid tissues and limit trafficking of induced ILC2s (Matloubian, Lo et al. 2004, Huang, Mao et al. 2018). FTY720-treated mice had the expected reduction of circulating total white blood cells, but showed no difference in psoriasis phenotype induction upon IL-23 administration compared with untreated controls, in both WT or *Rag1*$^{-/-}$ (lacking T and B cells) mice (**Fig. 1C and E**). Thus, in contrast to a model of lung inflammation (Huang, Mao et al. 2018), in psoriasis, tissue-resident ILCs are sufficient to drive disease pathology and are critical for amplifying the response to IL-23.

We observed that skin ILCs expressed the type 2 cytokines IL-5 and IL-13 in steady state, but showed potential to plastically to assume ILC3-like states. Consistent with prior reports that naïve mouse skin ILCs are comprised almost exclusively of GATA3^{+} ILC2s (Roediger, Kyle et al. 2013), total ILCs isolated from healthy mouse skin and treated with the type 2 alarmin cytokines IL-25

118 and L-33 had a strong type 2 activation, as indicated by expression of *Areg* and *Il13* (**Fig. S1D**).
119 However, total ILCs treated with IL-23 and IL-1β instead strongly expressed *Il22* and *Il17a* (**Fig.**
120 **S1D**), suggesting that tissue-resident skin ILCs may have potential for type 2-3 plasticity. Such
121 plasticity has been previously reported in IL-17A co-expressing "inflammatory ILC2s" in the lung
122 (Huang, Guo et al. 2015, Zhang, Xu et al. 2017), similar to reported type 3-1 plasticity in gut and
123 tonsil ILCs and type 2-1 plasticity in blood ILCs (Cella, Otero et al. 2010, Bernink, Krabbendam
124 et al. 2015, Bal, Bernink et al. 2016, Lim, Menegatti et al. 2016, Ohne, Silver et al. 2016, Silver,
125 Kearley et al. 2016). Moreover, while inflammation and skin thickness reverted to near-baseline
126 levels within 10 days after the initial IL-23 injection (**Fig. 1F**), this initial challenge promoted a
127 stronger type 3 response upon re-challenge. Specifically, mice showed a significantly more severe
128 phenotype after a second series of IL-23 injections, compared to their initial response (**Fig. 1F and**
129 **G**). This was also observed in mice treated with FTY720 during the primary injection (**Fig. S1E**),
130 suggesting that the plastic psoriatic response is not due to ILC recruitment.
131
132 We hypothesized that this plasticity may be encoded epigenetically. To test this hypothesis, we
133 profiled sorted total skin ILC populations from naïve mice by ATAC-seq. We observed the
134 expected open chromatin signature at the TSS of *Gata3*, *Il5* and *Il13* and not at the TSS of *Tbx21*
135 or *Rorc,* which encode T-bet and Rorγt, the hallmark transcription factors (TFs) of ILC1s and
136 ILC3s, respectively, or at the TSS of *Il22*, *Il17a*, or *Il17f* (**Fig. S1F and G**). In support of our
137 hypothesis, we also observed strong ATAC-seq peaks at at promoters of some type 3 genes in TFs
138 binding sites, such as *Batf, Maf,* and *Irf* (Ciofani, Madar et al. 2012, Li, Spolski et al. 2012, Zhong,
139 Cui et al. 2016) (**Fig. 1H**, **Fig. S1G)**, which are known to regulate Th17 cells. Taken together, our
140 data support a model where IL-23 induces psoriasis by remodeling a heterogeneous, tissue-resident

141 ILC population with unexpected potential for differentiation, rather than by recruiting circulating
142 ILCs to replace a homogenous, terminally differentiated skin-resident ILC2 population.
143
144 To assess the molecular heterogeneity of skin-resident ILCs and its functional implications for the
145 IL-23 response, we collected massively parallel scRNA-seq profiles from sorted pure total ILCs
146 from WT and *Rag1*$^{-/-}$ mice from naïve and IL-23 induced conditions, predominantly uncovering a
147 large heterogeneous population of cells (**Fig. 1I**). Specifically, clustering on principle components,
148 followed by differential expression analysis (**Methods**), identified a few discrete subsets of cells,
149 including a *Rag1*$^{-/-}$-specific subset (*A*), a cluster of proliferating cells from all conditions and
150 genotypes (*B*), and a cluster specific to the induced condition with very high *Il22* expression and
151 some *Il13* expression (*C*) (**Fig. 1J, Fig. S1H**). However, the vast majority of cells (81%) formed a
152 single, large heterogeneous and continuous "cloud" (*D*), which was not simply driven by technical
153 factors (**Methods**), with multiple sub-regions enriched for specific functional programs, including
154 type 2 immune response (**Fig. 1J**). Importantly, no single partitioning conformed to the expression
155 of key genes and processes, and moreover, some biological processes were unexpectedly shared
156 across subsets of the cells from distinct clusters (**Fig. 1J**). This highlighted the diversity of potential
157 cell states, and the need to capture them by more nuanced computational analysis.
158
159 To characterize the heterogeneity of ILCs during IL-23 response, we created a generative topic
160 model based on LDA. Analogous to a text document, a cell is modeled as a mixture of a small
161 number of topics, where the mixture weights indicate the relative prominence of the corresponding
162 biological process in that cell. Multiple topics may include the same gene, reflecting the gene's
163 roles in different processes. Topic modeling permits a cell to have multiple, non-hierarchical

164 "identities" that potentially differ in importance, a feature particularly relevant for analyzing
165 cellular plasticity (**Fig. 2A**). Indeed, we observed complex patterns of topic sharing across clusters,
166 suggesting that topic weights capture relationships not well described by clusters and, through their
167 functional interpretation, enable a more nuanced view of similarities and differences among cells
168 (**Fig. 2B**). Several choices for the number of topics may result in valid models, though too large a
169 number of topics can result in overfitting and low interpretability. We found that in this dataset,
170 15 topics captured important changes during disease induction, as well as other signals, without
171 obvious signs of overfitting (**Fig. S2A**, **Methods**).
172
173 Our topics spanned three categories: (**1**) highly ribosomal- or mitochondrial-dominated (*e.g.*,
174 Topic 1, 6), possibly reflecting technical quality or cell size, (**2**) cluster-specific topics (*e.g.*, Topic
175 7, 14, 15), and (**3**) "sub-regional" topics, that is, those featured in sub-regions of the "cloud", also
176 often simultaneously present in sub-regions of other clusters (*e.g.*, Topics 2, 4, 8, 11, 13) (**Fig. 2C**
177 **and D**, **Fig. S2B–D**). "Cell quality" topics can help distinguish the influence of technical
178 confounders better than simple thresholds, but also may reflect a cell's level of biological
179 activation (Wallrapp, Riesenfeld et al. 2017). "Cluster-specific topics" are analogous to results
180 from standard differential expression analysis. For example, cluster *C* is unique in having large
181 weights for Topic 15, which is characterized by expression of ILC3-associated genes *Il22, Il17a,*
182 and *Il17f,* as well as the cytotoxic gene *Gzmb* and the type 2 genes *Ly6a* (Sca-1) and *Il13* (**Fig. 2C**
183 **and D**, **Fig. S2B and C**). As another example, Topic 7 is uniquely highly weighted in cells from
184 the *Rag1*$^{-/-}$-specific cluster *A*, and features the NK-associated genes *Klrd1* and *Tyrobp* and the
185 immunoglobulin E receptor *Fcer1g,* indicating that *Rag1*$^{-/-}$ mice might have an overrepresentation
186 of skin-resident ILC1s (**Fig. 1J**, **Fig. S2D**).

187

188 The “sub-regional” topics highlighted functional states that are prominent within the “cloud” and
189 span across cluster boundaries, showing that ILCs from untreated skin span a spectrum of immune
190 states, including one characterized by *Vps37b* expression (Topic 2), a naïve/quiescent-like state
191 (Topic 8) and an activated state related to antigen presentation (Topic 11). Notably, this may mirror
192 "functional compartmentalization" reported in gut ILCs in homeostasis (Gury-BenAri, Thaiss et
193 al. 2016). This spectrum shifted upon disease induction, giving rise to greater representation of
194 classical *Il5*- and *Il13*-expressing “ILC2s” (Topic 13), as well as a mixed ILC2/ILC3-like state
195 characterized by strong expression of *Il13*, *Il17*, and *Il22* (Topic 15) (**Fig. 2C and D, Fig. S2B**).
196 Specifically, Topic 2, mainly present in the “cloud”, distinguishes between the untreated and
197 induced conditions, partly through ribosomal genes that may reflect differences in size between
198 naïve and activated cells (**Fig. 2C**). Topic 8 is characterized by expression of TFs previously
199 associated with both T- or B-cell quiescence, such as *Klf2/Klf4* (Carlson, Endrizzi et al. 2006, Cao,
200 Sun et al. 2010) and *Zfp36l2* (Galloway, Saveliev et al. 2016, Salerno, Engels et al. 2018), and
201 with repression of Th17 genetic programs, such as *Tsc22d3* (Yosef, Shalek et al. 2013), and may
202 thus reflect an actively maintained quiescent ILC state (ILC0) (**Fig. 2C and D**, **Fig. S2C**). Topic
203 11, which is present in cells from both WT conditions and the *Rag1*$^{-/-}$ induced condition, features
204 genes associated with antigen presentation, including MHCII invariant chain and MIF receptor
205 *Cd74(Schroder 2016)* and *Cd83* (Kuwano, Prazma et al. 2007), and type 2 ILCs (e.g., *Il13, Ccl1,*
206 and *Dgat2*, though not *Il5*) (Robinette, Fuchs et al. 2015, Gury-BenAri, Thaiss et al. 2016,
207 Wallrapp, Riesenfeld et al. 2017, Ricardo-Gonzalez, Van Dyken et al. 2018) (**Fig. 2C and D**).
208 Topic 13, highlighting a substantial sub-region of both the “cloud” and induced-specific cluster *C*,
209 is more specific to WT disease induction, uniquely expresses *Il5*, and also includes other type 2

210 genes, such as *Cxcl2*, *Il1rl1* (ST-2), *Il13*, and *Ly6a* (Sca-1), the latter of which featured in all
211 induced topics (**Fig. 2C and D**, **Fig. S2B and C**). The presence of some cells with high weights
212 for both Topics 13 and 15 indicates that an activated type 2 response apparently co-exists with the
213 anticipated type 3 response. Finally, Topic 4, which is largely mutually exclusive with Topic 13
214 across cells, includes genes involved in actin remodeling, a process previously shown to be
215 important during T-cell activation (Kumari, Curado et al. 2014) (**Fig. 2C and D**).
216
217 We hypothesized that cells can transition between some of these programs or states, as such
218 transitions would be consistent with the dense transcriptional continuum observed. Unlike
219 pseudotime inference (Trapnell, Cacchiarelli et al. 2014, Haghverdi, Buttner et al. 2016), topic
220 modeling does not assume the existence of an "axis" of progression, which may not exist in settings
221 such as the untreated condition. Moreover, when a trajectory does exist, it may be reflected only
222 in specific aspects of the transcriptional profiles. Indeed, a temporal "induction" dimension in our
223 data was revealed most clearly when we focused on specific topics related to immune repression
224 or activation. To identify transitional relationships in the context of the biological processes
225 reflected by these topics, we created a diffusion map only from those cells highly weighted for
226 Topics 2,4,8,11,13, and 15, but not for Topics 6 or 7, and used only the most distinguishing genes
227 for each topic as input (**Fig. S3A-C**, **Methods**).
228
229 The diffusion map (**Fig. 3A, Fig. S3D**) proposes several parallel state transitions that cells undergo
230 in the tissue, in particular highlighting a quiescence-ILC2-ILC3s state trajectory in the disease.
231 **First**, cells from the naïve condition lie in a triangular region in the plane spanned by diffusion
232 components (DC) 2 and 3 with corners up-weighted for Topic 2 ("resting"), 8 ("naïve-quiescent"),

233 and 11 ("antigen presentation"), respectively (**Fig. 3A and B.i–iii**). Their distribution throughout
234 the triangle suggests that in the untreated condition, cells range over all mixtures of these states.
235 **Second**, DC1 captures the induced response shared in both WT and *Rag1*$^{-/-}$ mice (**Fig. 3A, Fig.**
236 **S3D**), such that as their DC1 coordinate ("induction") increases, cells typically have relatively
237 lower weights for Topics 2, 8, and 11 (**Fig. 3B.i–iii, Fig. S3E.i-iii),** and higher weights for Topic
238 15 ("*Il22/Il117*"), Topic 4 ("actin remodeling"), and, specifically for cells from WT mice, Topic
239 13 ("*Il5/Cxcl2*") (**Fig. 3B.iv-vi**, **Fig. S3E.iv-vi**). Genotype-specific differences in the induction
240 response are further captured by DC4, such that cells from WT and *Rag1*$^{-/-}$ mice have increasingly
241 different DC4 coordinates as DC1 coordinate increases (**Fig. S3D**).
242
243 A focused diffusion map model (**Fig. 3C**) generated only from cells up-weighted for Topic 8, 13,
244 or 15 (**Methods**), shows continuous expression changes from Topic 8 to 13 to 15, as DC 1 (in this
245 map) coordinate increases (**Fig. 3D and E**). Indeed, DC1 is particularly well correlated with
246 expression of the gene *Srgn*, a proteoglycan that is critical for the trafficking and storage of *Gzmb*
247 (Sutton, Brennan et al. 2016), which suggests that expression of this gene could be an early
248 indicator of a trajectory toward type 3 activation, visible before expression of either *Gzmb* or type
249 3 cytokines (**Fig. 3E**). The expression changes observed across Topic 8, 13, and 15 are consistent
250 with a novel model of immune activation in which a type 3 stimulus (IL-23) causes skin-resident
251 naïve/quiescent ILCs to undergo type 2 activation, followed by transition to ILC3-like cells.
252
253 Finally, we tested the model's predictions of a quiescent-ILC2-ILC3 trajectory. First, we validated
254 the quiescent state by ATAC-Seq of sorted total skin ILC populations from naïve mice. Consistent
255 with Topic 8 ("naïve-quiescent") highlighted by the scRNA-seq analysis, the loci for the TFs *Klf2,*

256 *Klf4*, previously associated with quiescence (Carlson, Endrizzi et al. 2006, Cao, Sun et al. 2010),
257 *Tsc22d3* and *Zfp36l2,* associated with Th17 genetic program repression (Yosef, Shalek et al. 2013,
258 Galloway, Saveliev et al. 2016, Salerno, Engels et al. 2018) and *Cebpb*, involved in hematopoiesis
259 (Tsukada, Yoshida et al. 2011), had open chromatin signatures at their TSS (**Fig. 4A**).
260
261 Next, we tested the prediction of a transition during disease of IL-5–expressing ILC2s into IL-
262 22/IL-17A–expressing ILC3-like cells. We generated an IL-5 fate reporter mouse from IL-5-cre-
263 dTomato (Red5) (Nussbaum, Van Dyken et al. 2013) and Rosa26$^{\text{flox-Stop-floxYFP}}$, which we then
264 combined with IL-17A^{GFP} (Esplugues, Huber et al. 2011) and IL-22^{BFP} expression reporters (**Fig.**
265 **4B**). Consistent with our model, after IL-23 injection, ~10% of the IL-22– and IL-17A–expressing
266 cells were indeed ex-IL-5 producing cells, as measured by fate mapping of ILC2s, and a second
267 IL-23 challenge further elevated the number of ex-IL-5 cells producing IL-22 and IL-17A (**Fig.**
268 **4C and D**). Moreover, cells that expressed ILC3 type cytokines no longer expressed IL-5 (**Fig.**
269 **4D**). Our results show the *in vivo* potential for plasticity among skin ILCs and demonstrates that
270 some cells expressing ILC3 type cytokines expressed IL-5 at one stage of their lifetime. Finally,
271 we also tested our model's prediction that there is a subset of skin ILCs in the psoriasis model that
272 co-expresses the type 2 cytokine IL-13 with both of the type 3 cytokines IL-22 and IL-17A. Indeed,
273 intracellular measurements of these three cytokines showed that, consistent with the predictions,
274 nearly 20% in *Rag1*$^{-/-}$ and 10% in WT and *Tcrd*$^{-/-}$ of cells expressing IL-22 and IL-17A also co-
275 express IL-13 (**Fig. 4E and F**).
276
277
278

279 **DISCUSSION**

280 Experimentally combining scRNA-seq, ATAC-seq, and *in vivo* fate mapping in the psoriasis
281 mouse model with new analytical approaches, we showed the presence of previously undescribed
282 naïve/quiescent-like tissue-resident ILCs and the ability of activated ILC2s to differentiate to
283 pathological ILC3s. We further discovered a novel subset of ILCs expressing IL-13 and IL-22/IL-
284 17A in response to IL-23 stimulation. Our work highlights the limitation of experimental and
285 computational analyses of immune cells that treat them as discrete immune "types", when immune
286 cells may share biological signals and span continuous spectra. In our system, we did not observe
287 any discrete boundaries in single-cell expression profiles that neatly partitioned naïve/quiescent-
288 like ILCs from activated type 2 cells, or type 2 cells from type 3 cells. Rather, the entire population
289 of skin-resident ILCs was functionally reconfigured and its spectrum shifted by disease induction.
290 Indeed, imposing stress on an immune cell population may allow rapid shifting of such a spectrum
291 towards alternative cell fates (Tusi, Wolock et al. 2018), and pathways similar to those we
292 uncovered in the skin may play roles in other tissues. Importantly, this also suggests that studies
293 of ILCs sorted on expression of specific cytokines, such as IL-5 (Ricardo-Gonzalez, Van Dyken
294 et al. 2018), may not have fully assessed this larger continuum. This model substantially revises
295 previous interpretations and can provide a unified framework for some observations in other
296 systems, such as "functional compartmentalization" within ILC types and gut ILCs that could not
297 be readily assigned to a single ILC type (Gury-BenAri, Thaiss et al. 2016). These studies did not
298 report a differentiation from ILC2 to ILC3, (but rather reported that a core ILC2 module was robust
299 to antibiotic perturbation, albeit with increased expression of genes associated in homeostasis with
300 ILC3s (Gury-BenAri, Thaiss et al. 2016), which may reflect tissue-specific differences in ILC
301 features (Ricardo-Gonzalez, Van Dyken et al. 2018). Computational models and biological

302 interpretations that allow for such fluidity, including topic modeling, are thus valuable for
303 uncovering biological phenomena because they highlight signals, such as, in our case, type 2
304 activation, shared by cells in distinct clusters, and reveal drivers of heterogeneity among cells
305 within a single group, such as the ILC "cloud". This type of presentation is consistent with recent
306 studies of HSCs, where individual precursors have probabilistic fate maps, tilted towards but not
307 commited to specific outcomes (Carrelha, Meng et al. 2018, Laurenti and Gottgens 2018). Such
308 approaches should be valuable in uncovering how tissue-resident ILCs, and other cell types, may
309 globally respond to a stimulus, and undergo dynamic, plastic activation to reach the necessary state
310 for shaping the tissue landscape.

311 **METHODS**

312

313 **Mice.** C57BL/6, *Tcrd*$^{-/-}$ and Rosa26$^{flox\text{-}stop\text{-}floxYFP}$ Ai3(RCL-EYFP) mice were purchased from the
314 Jackson Laboratories. *Rag1*$^{-/-}$ and *Rag2*$^{-/-}$*IL2rg*$^{-/-}$ were purchased from Taconic Biosciences. IL-5
315 Cre, dTomato (Red5/R5) from Dr Locksley laboratory. The IL-5 fate reporter in this work was
316 generated by crossing Red5 with Ai3(RCL-EYFP) with IL-17A^{GFP} (Esplugues, Huber et al. 2011)
317 and IL-22^{BFP} generated in our laboratory. In order to maximize the Cre recombination and increase
318 the signal of Rosa26^{YFP} positive cells, we used homozygous IL-5^{dTomato,Cre}. We observed little to
319 no difference in IL-23 induced skin thicknening (**Fig. S4A**).

320

321 All mice were kept under specific pathogen-free (SPF) conditions in the animal facility at Yale
322 University. Age- and sex-matched littermates between 10 to 14 weeks of age were used for all
323 experiments. Unless with special instructions, mice were randomly assigned to different
324 experimental groups and each cage contained animals of all different experimental groups. Both
325 male and female mice were used in experiments. Animal procedures were approved by the
326 Institutional Animal Care and Use Committee (IACUC) of Yale University. Preliminary
327 experiments were tested to determine sample sizes, taking available recourses and ethical use into
328 account.

329

330 **Psoriasis model**

331 The psoriasis model used in this study is based on rIL-23 subcutaneous injections. The 500ng in
332 20µl of rIL-23 (provided by Abbvie or purchased from R&D Systems [scRNAseq experiments])
333 was injected daily into the ear skin of anesthetized mice in 4 consecutive days. As a control 20µl
334 of PBS was used with the same injection intervals. For the second challenge experiment, we waited

335 10 days, monitoring the skin thickness before repeating 4-day injection regimen. Skin thickness
336 was measured daily with calipers. When indicated, FTY720 (1mg/kg) was dissolved in PBS and
337 administered i.p on day -1, 1 and 3 of the experiment. Skin tissue was collected on day 5 for
338 histology imaging, flow cytometry analysis or cell sorting.
339
340 **Isolation of skin lymphocytes**
341 Ventral and dorsal dermal sheets of ears were separated, minced and incubated in RPMI medium
342 containing 0.4mg ml^{-1} Liberase TM (Roche Diagnostics) and 60ng/ul DNAseI (Sigma). After
343 digestion, the suspension was passed through and further mechanically disrupted with syringe
344 plunger and a 70uM cell strainer. Lymphocytes were enriched by gradient centrifugation in 27.5%
345 Optiprep solution (Sigma) and RPMI medium containing 5% Fetal Bovine Serum. Spleens were
346 mechanically disrupted using a syringe plunger in complete RPMI. Cells were filtered through 70-
347 μm nylon mesh and washed
348
349 **Flow cytometry and cell sorting**
350 Mouse ILCs were stained with monoclonal antibodies to CD45.2, CD90.2, lineage (CD4, CD8,
351 CD11b, CD11c, CD19, B220, NK1.1, Ter119, Gr1, FcEr1a), TCRβ, TCRγ, CD3ε. For
352 intracellular cytokine staining, cells were re-stimulated for 6 h at 37°C with phorbol 12-
353 myristate 13-acetate (PMA) (Sigma, 50 ng ml^{-1}) and ionomycin (Sigma, 1 μg ml^{-1}) in the
354 presence of Golgistop (BD Bioscience) added after initial 2h of stimulation. Next, cells were
355 fixed and stained with BS Cytofix/Cytoperm reagent (BD Biosciences) according to the
356 manufacturer's protocol. Intracellular cytokines were stained with antibodies to IL-13, IL-17A

357 and IL-22. Total ILCs were sorted as live, CD45+, CD90+, lin- (CD4, CD8, CD11b, CD11c,
358 CD19, B220, NK1.1, Ter119, Gr1, FcEr1a), CD3ε- and TCRγ/δ- cells into PBS/0.2%FBS.
359
360 ***In-vitro* ILC cultures**
361 For *in vitro* experiments, 5,000 ILCs were cultured per well of a 96-well round bottom plate in
362 Click's medium with 10 ng ml^{-1} IL-2 (R&D Systems) and 25 ng ml^{-1} IL-25 (R&D Systems) with
363 10 ng ml^{-1}, IL-33 (R&D Systems) or IL-23 25 ng ml^{-1} (Provided by Abbvie) with TGFβ 10 ng ml^{-}
364 ^{1} (R&D Systems) and IL-1β 10 ng ml^{-1} (R&D Systems). Cells were collected for RNA extraction
365 and qRT-PCR after 5 days of culture in 37°C and 5%CO_2.
366
367 **Adoptive ILC transfer**
368 Total skin ILCs were FACS purified and collected to PBS 5% serum. Cells were washed twice
369 with 1x PBS and injected (10,000 cells per mouse in 100ul) into retro-orbital vein of anesthetized
370 *Rag2*$^{-/-}$*IL2rg*$^{-/-}$ mice. IL-23 injection experiments were performed 14 days after the transfer.
371
372 **RNA extraction and Quantitative Real time PCR (qRT-PCR)**
373 RNA from *in vitro* cultures was isolated with RNeasy Mini Kit (QIAGEN) and qPCR was
374 performed using KAPA Probe Fast qPCR Master Mix 2x Kit (Kapa Biosystems, Wilmington, MA)
375 with TaqMan probes (Applied Biosystems) in a StepOne cycler (Applied Biosystems, Carlsbad,
376 CA). The CT values from duplicate qPCR reactions were extracted from the StepOne cycler
377 (Applied Biosystems, Carlsbad, CA) onto Excel spreadsheets and were analysed with the relative
378 quantification method $2^{\Delta\Delta CT}$.
379

380 **ATAC-seq**

381 Total ILCs sorted from naïve wild type mice were processed for ATAC-seq analysis according to
382 previously published protocol (Buenrostro, Giresi et al. 2013) with the low cell number input
383 version (~5,000 ILCs). Libraries from two independent experiments were sequenced on
384 HiSeq2500 with 75bp paired end reads. Each sample was sequenced to a depth of 150 million
385 reads.

386

387 **ATAC-Seq data analysis**

388 Adapter sequences were trimmed using FASTX-Toolkit (version 0.0.13,
389 http://hannonlab.cshl.edu/fastx_toolkit/) , after which Bowtie2 (Langmead and Salzberg 2012)
390 was used to align the reads to the mm10 genome. Picard tools (version 2.9.0,
391 https://broadinstitute.github.io/picard/) were used to remove PCR duplicates. Bedtools was used
392 to convert the bam file to a bed file, and all mapped reads were offset by +4 bp for the positive
393 strand and −5 bp for the negative strand. Peaks were called for each sample using macs2 (Zhang,
394 Liu et al. 2008) using parameters --nomodel --nolambda --shiftsize 75. ATAC-seq peaks were
395 visualizaed with the Integrative Genomics Viewer (Robinson, Thorvaldsdottir et al. 2011,
396 Thorvaldsdottir, Robinson et al. 2013) along with publicly available ChIP-seq via Cistrome DB
397 (Liu, Ortiz et al. 2011).

398

399 **Single cell RNA-Seq**

400 Sorted cells were washed with PBS/0.04% BSA and processed for droplet-based 3′ end massively
401 parallel scRNA-seq: sorted ILCs were encapsulated into droplets, and libraries were prepared

402 using Chromium Single Cell 3′ Reagent Kits v2 according to the manufacturer's protocol (10X
403 Genomics). scRNA-seq libraries were sequenced using a 75 cycle Nextseq 500 high output V2 kit.
404
405 **Single cell RNA-Seq data analysis**
406 **Initial data processing and QC.** Gene counts were obtained by aligning reads to the mm10
407 genome using CellRanger software (v1.3) (10x Genomics).
408
409 To remove doublets and poor-quality cells, cells were excluded from subsequent analysis if they
410 were outliers in their sample of origin in terms of number of genes or number of unique molecular
411 identifiers (UMIs), which eliminated 5.8–7.9% of cells per sample (**Fig. S4B**), or outliers across
412 all samples in percentage of mitochondrial genes, which eliminated at most 0.5% of remaining
413 cells (**Fig. S4C**). Sample-specific cut-offs ranged from 575–2,400 genes per cell for the *Rag1*$^{-/-}$
414 untreated sample to 850–3,100 genes per cell for the WT induced sample.
415
416 **Normalization.** To normalize gene counts, we used a scaling factor that reflected the expected
417 number of UMIs in each sample (**Fig. S4D**), rather than scaling all cells to a constant size, as in
418 TPM (Wallrapp, Riesenfeld et al. 2017) Let w_s be the mean number of UMIs per cell in sample s.
419 UMI counts for cells in sample s were scaled to:
420 $10,000 \times (w_s / w_{\text{WT naive}})$
421 Taking the log of scaled UMI counts gives the normalized expression values referred to as logTPX.
422
423 **Determination of variable genes.** We fit the count data to a null model based on a negative
424 binomial distribution that explains the expected technical variation for each gene, given its

425 expression level, as previously described(Pandey, Shekhar et al. 2018). A gene was considered to
426 exhibit non-technical variability if it had mean counts above 0.005 and a coefficient of variation
427 at least log(0.5) times that predicted by the null model (**Fig. S4E**). We performed variable gene
428 selection separately for each sample as well as for pooled samples from WT mice and, separately,
429 from *Rag1*$^{-/-}$ mice. To reduce downstream technical effects of the variation in extremely highly
430 expressing genes, we then removed any genes that had mean counts above 4 in WT or, separately,
431 *Rag1*$^{-/-}$ cells (these were mostly ribosomal protein genes). The resulting conservative set of 271
432 genes was then used for the singular value decomposition (SVD). We chose this approach to ensure
433 that noisy variable gene selection was not a cause of the heterogeneity in the "cloud". Note that
434 downstream results were qualitatively similar and robust to several parameter settings, which yield
435 variable gene sets of very different sizes, as well as to other selection approaches (including the
436 FindVariableGenes() function in Seurat) (Butler, Hoffman et al. 2018).
437
438 **Dimensionality reduction, clustering, and visualization.** We computed an SVD on *z*-scored
439 variable genes, as determined above, using Seurat's RunPCA() function, with the "weight.by.var"
440 parameter set to FALSE (Butler, Hoffman et al. 2018). Assessing the decrease in marginal
441 proportion of variance explained with larger components, we selected the top 18 eigenvectors for
442 subsequent analysis, and confirmed that the resulting analyses were not sensitive to this exact
443 choice. We used these components with Seurat's FindClusters() and RunTSNE() functions, with
444 other parameter settings set to default, to cluster the cells, and to separately create a *t*-stochastic
445 neighborhood embedding (tSNE) for visualization, respectively. As previously described,
446 FindClusters() optimizes a modularity function on a *k*-nearest-neighbor graph computed from the
447 top eigenvectors.

448

449 **Removal of non-ILC clusters.** Based on expression of marker genes across clusters, we
450 determined that a few very distinct clusters were unlikely to be ILCs: cells in those clusters had
451 little expression of *Ptprc* (CD45), and high expression of *Col1a2*, or *Tie1* and *Pecam1,* or *Krt15.*
452 Cells from these non-ILC clusters were removed, and the steps of normalizing the data, selecting
453 variable genes, performing PCA, and creating a tSNE were repeated as before, but the top 20
454 components of the SVD were used for subsequent analysis. After these steps, 18,852 cell profiles
455 remained, with 4,619–4,857 cells per sample.

456

457 **Topic modeling.** We fit an LDA topic model on the full, sparse counts matrix (18,852 cells and
458 27,998 genes) using the FitGoM() function from the CountClust R package (Dey, Hsiao et al.
459 2017), with the number of clusters *K* set to 15 and the "tol" tolera˜nce parameter set to 10. This
460 package is heavily based on the maptpx R package, which implements a posterior maximization
461 approach to fitting the model (Taddy 2012). Some approaches to selecting an appropriate value of
462 *K* rely on having labeled training data for the model. Since we do not have such a model, we fit
463 the model for a range of values and computed the Akaike and Bayesian information criteria (AIC
464 and BIC) using the estimated likelihood returned by FitGoM() (**Fig. S2A**). Since AIC and BIC risk
465 under- and over-penalizing the fit, respectively, we selected a value of *K* at a point where the AIC
466 curve had begun to decrease less steeply and the BIC curve had begun to climb.

467

468 **Diffusion maps**. To select cells and genes for the construction of diffusion maps, a cell was
469 considered "highly weighted" for a topic if its weight for the topic was above a topic-specific
470 threshold capturing the upper tail of the distribution (**Fig. S3A and B**). The analysis is not sensitive

471 to the exact choice of threshold. Cells were used in the large diffusion map (**Fig. 3A**) if they were
472 highly weighted for any of topics 2, 4, 8, 11, 13, or 15, but not 6 or 7 (**Fig. S3B and C**). A gene
473 was considered to be in the "top *n* genes" for a topic if it was returned by the CountClust function
474 ExtractTopFeatures(), which selects genes that are most critical for separating one topic from the
475 others (similar to differential expression analysis between clusters), with the following parameter
476 settings: top_features=*n,* method="poisson", options="min", shared=TRUE. For visualization, the
477 "Score" shown for top genes (**Fig. 2C, Fig. S2D**) was computed as 100**x,* where *x* is the Kullback-
478 Leibler divergence score output by ExtractTopFeatures(), and then plotted on a logarithmic scale.
479 Genes were included in the large diffusion map if they were in the top 50 genes for topics 2, 4, 8,
480 11, 13, or 15, but not in the top 5 genes for any other topics. For the smaller diffusion map (**Fig.**
481 **3C**), cells and genes were selected in an analogous way, but only for the three topics 8, 13, and 15.
482 Overall, the larger diffusion map was computed on 7,888 cells and 245 genes, and the smaller one
483 on 3,785 cells and 130 genes. To build the diffusion map, we gave the expression data for these
484 cells and genes as input to the DiffusionMap() function from the destiny R package (Angerer,
485 Haghverdi et al. 2016), with parameter settings *k*=50 and sigma="local".
486

487 **Acknowledgments**

488 We would like to thank Ania Hupalowska and Leslie Gaffney for help in manuscript preparation.
489 This work was supported in part by grants (YAP-013-2015) provided by AbbVie (RAF, PB). Work
490 supported by the Klarman Cell Observatory (AR) and HHMI (AR and RAF). AR is an SAB
491 member of ThermoFisher Scientific, Syros Pharmaceuticals, and Driver Group and a founder of
492 Celsius Therapeutics.
493

494 **References**

495 Ahn, J., Y. Yuan, G. Parmigiani, M. B. Suraokar, L. Diao, Wistuba, II and W. Wang (2013). "DeMix:
496 deconvolution for mixed cancer transcriptomes using raw measured data." Bioinformatics
497 **29**(15): 1865-1871.
498 Angerer, P., L. Haghverdi, M. Buttner, F. J. Theis, C. Marr and F. Buettner (2016). "destiny:
499 diffusion maps for large-scale single-cell data in R." Bioinformatics **32**(8): 1241-1243.
500 Bal, S. M., J. H. Bernink, M. Nagasawa, J. Groot, M. M. Shikhagaie, K. Golebski, C. M. van
501 Drunen, R. Lutter, R. E. Jonkers, P. Hombrink, M. Bruchard, J. Villaudy, J. M. Munneke, W.
502 Fokkens, J. S. Erjefalt, H. Spits and X. R. Ros (2016). "IL-1beta, IL-4 and IL-12 control the fate of
503 group 2 innate lymphoid cells in human airway inflammation in the lungs." Nat Immunol **17**(6):
504 636-645.
505 Bernink, J. H., L. Krabbendam, K. Germar, E. de Jong, K. Gronke, M. Kofoed-Nielsen, J. M.
506 Munneke, M. D. Hazenberg, J. Villaudy, C. J. Buskens, W. A. Bemelman, A. Diefenbach, B. Blom
507 and H. Spits (2015). "Interleukin-12 and -23 Control Plasticity of CD127(+) Group 1 and Group 3
508 Innate Lymphoid Cells in the Intestinal Lamina Propria." Immunity **43**(1): 146-160.
509 Blei, D. M., Ng, A.Y., Jordan, M.I. (2003). "Latent Dirichlet Allocation." Journal of Machine
510 Learning Research **3**: 29.
511 Buenrostro, J. D., P. G. Giresi, L. C. Zaba, H. Y. Chang and W. J. Greenleaf (2013). "Transposition
512 of native chromatin for fast and sensitive epigenomic profiling of open chromatin, DNA-binding
513 proteins and nucleosome position." Nat Methods **10**(12): 1213-1218.
514 Butler, A., P. Hoffman, P. Smibert, E. Papalexi and R. Satija (2018). "Integrating single-cell
515 transcriptomic data across different conditions, technologies, and species." Nat Biotechnol
516 **36**(5): 411-420.
517 Cai, Y., X. Shen, C. Ding, C. Qi, K. Li, X. Li, V. R. Jala, H. G. Zhang, T. Wang, J. Zheng and J. Yan
518 (2011). "Pivotal role of dermal IL-17-producing gammadelta T cells in skin inflammation."
519 Immunity **35**(4): 596-610.
520 Cao, Z., X. Sun, B. Icli, A. K. Wara and M. W. Feinberg (2010). "Role of Kruppel-like factors in
521 leukocyte development, function, and disease." Blood **116**(22): 4404-4414.
522 Carlson, C. M., B. T. Endrizzi, J. Wu, X. Ding, M. A. Weinreich, E. R. Walsh, M. A. Wani, J. B.
523 Lingrel, K. A. Hogquist and S. C. Jameson (2006). "Kruppel-like factor 2 regulates thymocyte and
524 T-cell migration." Nature **442**(7100): 299-302.
525 Carrelha, J., Y. Meng, L. M. Kettyle, T. C. Luis, R. Norfo, V. Alcolea, H. Boukarabila, F. Grasso, A.
526 Gambardella, A. Grover, K. Hogstrand, A. M. Lord, A. Sanjuan-Pla, P. S. Woll, C. Nerlov and S. E.
527 W. Jacobsen (2018). "Hierarchically related lineage-restricted fates of multipotent
528 haematopoietic stem cells." Nature **554**(7690): 106-111.
529 Cella, M., K. Otero and M. Colonna (2010). "Expansion of human NK-22 cells with IL-7, IL-2, and
530 IL-1beta reveals intrinsic functional plasticity." Proc Natl Acad Sci U S A **107**(24): 10961-10966.
531 Ciofani, M., A. Madar, C. Galan, M. Sellars, K. Mace, F. Pauli, A. Agarwal, W. Huang, C. N.
532 Parkhurst, M. Muratet, K. M. Newberry, S. Meadows, A. Greenfield, Y. Yang, P. Jain, F. K. Kirigin,
533 C. Birchmeier, E. F. Wagner, K. M. Murphy, R. M. Myers, R. Bonneau and D. R. Littman (2012).
534 "A validated regulatory network for Th17 cell specification." Cell **151**(2): 289-303.
535 Dey, K. K., C. J. Hsiao and M. Stephens (2017). "Visualizing the structure of RNA-seq expression
536 data using grade of membership models." PLoS Genet **13**(3): e1006599.

537 Dyring-Andersen, B., C. Geisler, C. Agerbeck, J. P. Lauritsen, S. D. Gudjonsdottir, L. Skov and C.
538 M. Bonefeld (2014). "Increased number and frequency of group 3 innate lymphoid cells in
539 nonlesional psoriatic skin." Br J Dermatol **170**(3): 609-616.
540 Esplugues, E., S. Huber, N. Gagliani, A. E. Hauser, T. Town, Y. Y. Wan, W. O'Connor, Jr., A.
541 Rongvaux, N. Van Rooijen, A. M. Haberman, Y. Iwakura, V. K. Kuchroo, J. K. Kolls, J. A.
542 Bluestone, K. C. Herold and R. A. Flavell (2011). "Control of TH17 cells occurs in the small
543 intestine." Nature **475**(7357): 514-518.
544 Galloway, A., A. Saveliev, S. Lukasiak, D. J. Hodson, D. Bolland, K. Balmanno, H. Ahlfors, E.
545 Monzon-Casanova, S. C. Mannurita, L. S. Bell, S. Andrews, M. D. Diaz-Munoz, S. J. Cook, A.
546 Corcoran and M. Turner (2016). "RNA-binding proteins ZFP36L1 and ZFP36L2 promote cell
547 quiescence." Science **352**(6284): 453-459.
548 Gasteiger, G., X. Fan, S. Dikiy, S. Y. Lee and A. Y. Rudensky (2015). "Tissue residency of innate
549 lymphoid cells in lymphoid and nonlymphoid organs." Science **350**(6263): 981-985.
550 Gury-BenAri, M., C. A. Thaiss, N. Serafini, D. R. Winter, A. Giladi, D. Lara-Astiaso, M. Levy, T. M.
551 Salame, A. Weiner, E. David, H. Shapiro, M. Dori-Bachash, M. Pevsner-Fischer, E. Lorenzo-Vivas,
552 H. Keren-Shaul, F. Paul, A. Harmelin, G. Eberl, S. Itzkovitz, A. Tanay, J. P. Di Santo, E. Elinav and I.
553 Amit (2016). "The Spectrum and Regulatory Landscape of Intestinal Innate Lymphoid Cells Are
554 Shaped by the Microbiome." Cell **166**(5): 1231-1246 e1213.
555 Haghverdi, L., M. Buttner, F. A. Wolf, F. Buettner and F. J. Theis (2016). "Diffusion pseudotime
556 robustly reconstructs lineage branching." Nat Methods **13**(10): 845-848.
557 Huang, Y., L. Guo, J. Qiu, X. Chen, J. Hu-Li, U. Siebenlist, P. R. Williamson, J. F. Urban, Jr. and W.
558 E. Paul (2015). "IL-25-responsive, lineage-negative KLRG1(hi) cells are multipotential
559 'inflammatory' type 2 innate lymphoid cells." Nat Immunol **16**(2): 161-169.
560 Huang, Y., K. Mao, X. Chen, M. A. Sun, T. Kawabe, W. Li, N. Usher, J. Zhu, J. F. Urban, Jr., W. E.
561 Paul and R. N. Germain (2018). "S1P-dependent interorgan trafficking of group 2 innate
562 lymphoid cells supports host defense." Science **359**(6371): 114-119.
563 Kumari, S., S. Curado, V. Mayya and M. L. Dustin (2014). "T cell antigen receptor activation and
564 actin cytoskeleton remodeling." Biochim Biophys Acta **1838**(2): 546-556.
565 Kuwano, Y., C. M. Prazma, N. Yazawa, R. Watanabe, N. Ishiura, A. Kumanogoh, H. Okochi, K.
566 Tamaki, M. Fujimoto and T. F. Tedder (2007). "CD83 influences cell-surface MHC class II
567 expression on B cells and other antigen-presenting cells." Int Immunol **19**(8): 977-992.
568 Langmead, B. and S. L. Salzberg (2012). "Fast gapped-read alignment with Bowtie 2." Nat
569 Methods **9**(4): 357-359.
570 Laurenti, E. and B. Gottgens (2018). "From haematopoietic stem cells to complex differentiation
571 landscapes." Nature **553**(7689): 418-426.
572 Li, P., R. Spolski, W. Liao, L. Wang, T. L. Murphy, K. M. Murphy and W. J. Leonard (2012). "BATF-
573 JUN is critical for IRF4-mediated transcription in T cells." Nature **490**(7421): 543-546.
574 Li, Z., T. Hodgkinson, E. J. Gothard, S. Boroumand, R. Lamb, I. Cummins, P. Narang, A. Sawtell, J.
575 Coles, G. Leonov, A. Reboldi, C. D. Buckley, T. Cupedo, C. Siebel, A. Bayat, M. C. Coles and C. A.
576 Ambler (2016). "Epidermal Notch1 recruits RORgamma(+) group 3 innate lymphoid cells to
577 orchestrate normal skin repair." Nat Commun **7**: 11394.
578 Lim, A. I., S. Menegatti, J. Bustamante, L. Le Bourhis, M. Allez, L. Rogge, J. L. Casanova, H. Yssel
579 and J. P. Di Santo (2016). "IL-12 drives functional plasticity of human group 2 innate lymphoid
580 cells." J Exp Med **213**(4): 569-583.

581 Lindsay, J., Mandoiu, I., Nelson, C. (2013). "Gene Expression Deconvolution using Single-cells."
582 Proceedings of the 2013 American Association of Human Genetics meeting.
583 Liu, T., J. A. Ortiz, L. Taing, C. A. Meyer, B. Lee, Y. Zhang, H. Shin, S. S. Wong, J. Ma, Y. Lei, U. J.
584 Pape, M. Poidinger, Y. Chen, K. Yeung, M. Brown, Y. Turpaz and X. S. Liu (2011). "Cistrome: an
585 integrative platform for transcriptional regulation studies." Genome Biol **12**(8): R83.
586 Matloubian, M., C. G. Lo, G. Cinamon, M. J. Lesneski, Y. Xu, V. Brinkmann, M. L. Allende, R. L.
587 Proia and J. G. Cyster (2004). "Lymphocyte egress from thymus and peripheral lymphoid organs
588 is dependent on S1P receptor 1." Nature **427**(6972): 355-360.
589 Nograles, K. E., L. C. Zaba, E. Guttman-Yassky, J. Fuentes-Duculan, M. Suarez-Farinas, I.
590 Cardinale, A. Khatcherian, J. Gonzalez, K. C. Pierson, T. R. White, C. Pensabene, I. Coats, I.
591 Novitskaya, M. A. Lowes and J. G. Krueger (2008). "Th17 cytokines interleukin (IL)-17 and IL-22
592 modulate distinct inflammatory and keratinocyte-response pathways." Br J Dermatol **159**(5):
593 1092-1102.
594 Nussbaum, J. C., S. J. Van Dyken, J. von Moltke, L. E. Cheng, A. Mohapatra, A. B. Molofsky, E. E.
595 Thornton, M. F. Krummel, A. Chawla, H. E. Liang and R. M. Locksley (2013). "Type 2 innate
596 lymphoid cells control eosinophil homeostasis." Nature **502**(7470): 245-248.
597 Ohne, Y., J. S. Silver, L. Thompson-Snipes, M. A. Collet, J. P. Blanck, B. L. Cantarel, A. M.
598 Copenhaver, A. A. Humbles and Y. J. Liu (2016). "IL-1 is a critical regulator of group 2 innate
599 lymphoid cell function and plasticity." Nat Immunol **17**(6): 646-655.
600 Pandey, S., K. Shekhar, A. Regev and A. F. Schier (2018). "Comprehensive Identification and
601 Spatial Mapping of Habenular Neuronal Types Using Single-Cell RNA-Seq." Curr Biol **28**(7): 1052-
602 1065 e1057.
603 Pantelyushin, S., S. Haak, B. Ingold, P. Kulig, F. L. Heppner, A. A. Navarini and B. Becher (2012).
604 "Rorgammat+ innate lymphocytes and gammadelta T cells initiate psoriasiform plaque
605 formation in mice." J Clin Invest **122**(6): 2252-2256.
606 Pritchard, J. K., M. Stephens and P. Donnelly (2000). "Inference of population structure using
607 multilocus genotype data." Genetics **155**(2): 945-959.
608 Quon, G., S. Haider, A. G. Deshwar, A. Cui, P. C. Boutros and Q. Morris (2013). "Computational
609 purification of individual tumor gene expression profiles leads to significant improvements in
610 prognostic prediction." Genome Med **5**(3): 29.
611 Repsilber, D., S. Kern, A. Telaar, G. Walzl, G. F. Black, J. Selbig, S. K. Parida, S. H. Kaufmann and
612 M. Jacobsen (2010). "Biomarker discovery in heterogeneous tissue samples -taking the in-silico
613 deconfounding approach." BMC Bioinformatics **11**: 27.
614 Ricardo-Gonzalez, R. R., S. J. Van Dyken, C. Schneider, J. Lee, J. C. Nussbaum, H. E. Liang, D.
615 Vaka, W. L. Eckalbar, A. B. Molofsky, D. J. Erle and R. M. Locksley (2018). "Tissue signals imprint
616 ILC2 identity with anticipatory function." Nat Immunol.
617 Robinette, M. L., A. Fuchs, V. S. Cortez, J. S. Lee, Y. Wang, S. K. Durum, S. Gilfillan, M. Colonna
618 and C. Immunological Genome (2015). "Transcriptional programs define molecular
619 characteristics of innate lymphoid cell classes and subsets." Nat Immunol **16**(3): 306-317.
620 Robinson, J. T., H. Thorvaldsdottir, W. Winckler, M. Guttman, E. S. Lander, G. Getz and J. P.
621 Mesirov (2011). "Integrative genomics viewer." Nat Biotechnol **29**(1): 24-26.
622 Roediger, B., R. Kyle, K. H. Yip, N. Sumaria, T. V. Guy, B. S. Kim, A. J. Mitchell, S. S. Tay, R. Jain, E.
623 Forbes-Blom, X. Chen, P. L. Tong, H. A. Bolton, D. Artis, W. E. Paul, B. Fazekas de St Groth, M. A.

624 Grimbaldeston, G. Le Gros and W. Weninger (2013). "Cutaneous immunosurveillance and
625 regulation of inflammation by group 2 innate lymphoid cells." Nat Immunol **14**(6): 564-573.
626 Salerno, F., S. Engels, M. van den Biggelaar, F. P. J. van Alphen, A. Guislain, W. Zhao, D. L.
627 Hodge, S. E. Bell, J. P. Medema, M. von Lindern, M. Turner, H. A. Young and M. C. Wolkers
628 (2018). "Translational repression of pre-formed cytokine-encoding mRNA prevents chronic
629 activation of memory T cells." Nat Immunol.
630 Schroder, B. (2016). "The multifaceted roles of the invariant chain CD74--More than just a
631 chaperone." Biochim Biophys Acta **1863**(6 Pt A): 1269-1281.
632 Schwartz, R. and S. E. Shackney (2010). "Applying unmixing to gene expression data for tumor
633 phylogeny inference." BMC Bioinformatics **11**: 42.
634 Shen-Orr, S. S., R. Tibshirani, P. Khatri, D. L. Bodian, F. Staedtler, N. M. Perry, T. Hastie, M. M.
635 Sarwal, M. M. Davis and A. J. Butte (2010). "Cell type-specific gene expression differences in
636 complex tissues." Nat Methods **7**(4): 287-289.
637 Silver, J. S., J. Kearley, A. M. Copenhaver, C. Sanden, M. Mori, L. Yu, G. H. Pritchard, A. A. Berlin,
638 C. A. Hunter, R. Bowler, J. S. Erjefalt, R. Kolbeck and A. A. Humbles (2016). "Inflammatory
639 triggers associated with exacerbations of COPD orchestrate plasticity of group 2 innate
640 lymphoid cells in the lungs." Nat Immunol **17**(6): 626-635.
641 Spencer, S. P., C. Wilhelm, Q. Yang, J. A. Hall, N. Bouladoux, A. Boyd, T. B. Nutman, J. F. Urban,
642 Jr., J. Wang, T. R. Ramalingam, A. Bhandoola, T. A. Wynn and Y. Belkaid (2014). "Adaptation of
643 innate lymphoid cells to a micronutrient deficiency promotes type 2 barrier immunity." Science
644 **343**(6169): 432-437.
645 Sutton, V. R., A. J. Brennan, S. Ellis, J. Danne, K. Thia, M. R. Jenkins, I. Voskoboinik, G. Pejler, R.
646 W. Johnstone, D. M. Andrews and J. A. Trapani (2016). "Serglycin determines secretory granule
647 repertoire and regulates natural killer cell and cytotoxic T lymphocyte cytotoxicity." FEBS J
648 **283**(5): 947-961.
649 Taddy, M. (2012). "On Estimation and Selection for Topic Models." Proceedings of Machine
650 Learning Research **22**: 1184--1193.
651 Teunissen, M. B., J. M. Munneke, J. H. Bernink, P. I. Spuls, P. C. Res, A. Te Velde, S. Cheuk, M. W.
652 Brouwer, S. P. Menting, L. Eidsmo, H. Spits, M. D. Hazenberg and J. Mjosberg (2014).
653 "Composition of innate lymphoid cell subsets in the human skin: enrichment of NCR(+) ILC3 in
654 lesional skin and blood of psoriasis patients." J Invest Dermatol **134**(9): 2351-2360.
655 Teunissen, M. B. M., J. M. Munneke, J. H. Bernink, P. I. Spuls, P. C. M. Res, A. Te Velde, S. Cheuk,
656 M. W. D. Brouwer, S. P. Menting, L. Eidsmo, H. Spits, M. D. Hazenberg and J. Mjosberg (2014).
657 "Composition of innate lymphoid cell subsets in the human skin: enrichment of NCR(+) ILC3 in
658 lesional skin and blood of psoriasis patients." J Invest Dermatol **134**(9): 2351-2360.
659 Thorvaldsdottir, H., J. T. Robinson and J. P. Mesirov (2013). "Integrative Genomics Viewer (IGV):
660 high-performance genomics data visualization and exploration." Brief Bioinform **14**(2): 178-192.
661 Trapnell, C., D. Cacchiarelli, J. Grimsby, P. Pokharel, S. Li, M. Morse, N. J. Lennon, K. J. Livak, T. S.
662 Mikkelsen and J. L. Rinn (2014). "The dynamics and regulators of cell fate decisions are revealed
663 by pseudotemporal ordering of single cells." Nat Biotechnol **32**(4): 381-386.
664 Tsukada, J., Y. Yoshida, Y. Kominato and P. E. Auron (2011). "The CCAAT/enhancer (C/EBP)
665 family of basic-leucine zipper (bZIP) transcription factors is a multifaceted highly-regulated
666 system for gene regulation." Cytokine **54**(1): 6-19.

667 Tusi, B. K., S. L. Wolock, C. Weinreb, Y. Hwang, D. Hidalgo, R. Zilionis, A. Waisman, J. R. Huh, A.
668 M. Klein and M. Socolovsky (2018). "Population snapshots predict early haematopoietic and
669 erythroid hierarchies." Nature **555**(7694): 54-60.
670 Villanova, F., B. Flutter, I. Tosi, K. Grys, H. Sreeneebus, G. K. Perera, A. Chapman, C. H. Smith, P.
671 Di Meglio and F. O. Nestle (2014). "Characterization of innate lymphoid cells in human skin and
672 blood demonstrates increase of NKp44+ ILC3 in psoriasis." J Invest Dermatol **134**(4): 984-991.
673 Villanova, F., B. Flutter, I. Tosi, K. Grys, H. Sreeneebus, G. K. Perera, A. Chapman, C. H. Smith, P.
674 Di Meglio and F. O. Nestle (2014). "Characterization of innate lymphoid cells in human skin and
675 blood demonstrates increase of NKp44+ ILC3 in psoriasis." J Invest Dermatol **134**(4): 984-991.
676 Wallrapp, A., S. J. Riesenfeld, P. R. Burkett, R. E. Abdulnour, J. Nyman, D. Dionne, M. Hofree, M.
677 S. Cuoco, C. Rodman, D. Farouq, B. J. Haas, T. L. Tickle, J. J. Trombetta, P. Baral, C. S. N. Klose, T.
678 Mahlakoiv, D. Artis, O. Rozenblatt-Rosen, I. M. Chiu, B. D. Levy, M. S. Kowalczyk, A. Regev and V.
679 K. Kuchroo (2017). "The neuropeptide NMU amplifies ILC2-driven allergic lung inflammation."
680 Nature **549**(7672): 351-356.
681 Wang, N., T. Gong, R. Clarke, L. Chen, M. Shih Ie, Z. Zhang, D. A. Levine, J. Xuan and Y. Wang
682 (2015). "UNDO: a Bioconductor R package for unsupervised deconvolution of mixed gene
683 expressions in tumor samples." Bioinformatics **31**(1): 137-139.
684 Yang, J., S. Hu, L. Zhao, D. H. Kaplan, G. H. Perdew and N. Xiong (2016). "Selective programming
685 of CCR10(+) innate lymphoid cells in skin-draining lymph nodes for cutaneous homeostatic
686 regulation." Nat Immunol **17**(1): 48-56.
687 Yosef, N., A. K. Shalek, J. T. Gaublomme, H. Jin, Y. Lee, A. Awasthi, C. Wu, K. Karwacz, S. Xiao, M.
688 Jorgolli, D. Gennert, R. Satija, A. Shakya, D. Y. Lu, J. J. Trombetta, M. R. Pillai, P. J. Ratcliffe, M. L.
689 Coleman, M. Bix, D. Tantin, H. Park, V. K. Kuchroo and A. Regev (2013). "Dynamic regulatory
690 network controlling TH17 cell differentiation." Nature **496**(7446): 461-468.
691 Zhang, K., X. Xu, M. A. Pasha, C. W. Siebel, A. Costello, A. Haczku, K. MacNamara, T. Liang, J.
692 Zhu, A. Bhandoola, I. Maillard and Q. Yang (2017). "Cutting Edge: Notch Signaling Promotes the
693 Plasticity of Group-2 Innate Lymphoid Cells." J Immunol **198**(5): 1798-1803.
694 Zhang, Y., T. Liu, C. A. Meyer, J. Eeckhoute, D. S. Johnson, B. E. Bernstein, C. Nusbaum, R. M.
695 Myers, M. Brown, W. Li and X. S. Liu (2008). "Model-based analysis of ChIP-Seq (MACS)."
696 Genome Biol **9**(9): R137.
697 Zhong, C., K. Cui, C. Wilhelm, G. Hu, K. Mao, Y. Belkaid, K. Zhao and J. Zhu (2016). "Group 3
698 innate lymphoid cells continuously require the transcription factor GATA-3 after commitment."
699 Nat Immunol **17**(2): 169-178.
700

Figure 1. An epigenetically poised, heterogenous population of tissue-resident ILCs drive initial IL-23–induced pathology. (A) Study overview. From left: Psoriasis mouse model is based on a series of subcutaneous IL-23 injections in WT, *Rag1*$^{-/-}$ and *Tcdr*$^{-/-}$ mice, phenotypic measurement of skin thickness, and tissue collection and cell isolation for assessment by scRNA-seq, in vitro assays and cytokine expression. (**B,C)** Tissue resident ILCs are necessary and sufficient for increase in ear skin thickness in response to IL-23 treatment. Increase in skin thickness (mm, y axis) over time (days, x axis) in (**B**) WT (black), *Rag1*$^{-/-}$ (lack all T and B cells, blue), *Rag2*$^{-/-}$ *Il2rg*$^{-/-}$ mice (also lack ILCs, magenta), and TCRγδ$^{-/-}$ (lack γδ T cells, grey) (n=7 for each group) as well as in (**C**) *Rag2*$^{-/-}$ *Il2rg*$^{-/-}$ mice with (blue) and without (black) intravenously transferred ILCs (n=4 for each group)**. (D)** FTY720 blocks white blood cell circulation. Total circulatory white blood cell (WBC) numbers (10^3/μl; y axis) in untreated ("Non-Tx") and FTY720-treated ("FTY720-Tx"), WT and Rag$^{-/-}$ mice. (**E)** IL23-dependent increases in ear skin thickness does not require circulating cells. Increase in skin thickness (mm, y axis) over time (days, x axis) following IL-23 treatment, in WT (top) and Rag$^{-/-}$ (bottom) mice, with (red) and without (black) FTY720-treatment (**Methods)** (n=3 WT both groups, n=2 *Rag1*$^{-/-}$ NonTX n=4 *Rag1*$^{-/-}$ FTY720). (**F,G**) A secondary challenge with IL-23 increases susceptibility. Increase in skin thickness (mm, y axis) over time (days, x axis; top) or at the end (bottom) of a primary (white bar) or secondary (blue bars) challenge with either IL-23 (n=14) or saline control (PBS) (n=5). (**H)** ILCs in untreated mice are epigenetically poised to become ILC3s. Mapped ATAC-seq reads (top track) at the *Il22* (left) and *Il5* (right) promoter loci (bottom track) from sorted skin ILCs from untreated mice, show open chromatin peaks (beige and blue bars) at key TF binding sites (beige), previously identified in CD4$^+$ T cell ChIP-seq data (middle tracks), and at the TSS of *Il5* but not *Il22* (blue). (**I,J)** ILC heterogeneity highlighted by scRNA-seq. *t*-Distributed stochastic neighbor embedding (tSNE) of 27,998 single cell (dots) profiles (**Methods**) colored by either *in vivo* treatment and genotype (**i**), or by cluster assignment or expression of key genes (color bar, logTPX (**Methods**)) (**J**). Annotated clusters (**J**, top left) include a *Rag1*$^{-/-}$-specific cluster (A) expressing the ILC1-associated gene *Klrd1*, cycling cells (B), an *Il22*-high cluster co-expressing *Il13* (C), and a heterogeneous "cloud" (D), without discrete boundaries between clusters yet with multiple patterns of graded gene expression. Error bars, SD; **p<0.021, ***p<0.0002, ****p<0.0001 by unpaired t test (b) or two-way ANOVA (d, e, g).

Figure 1

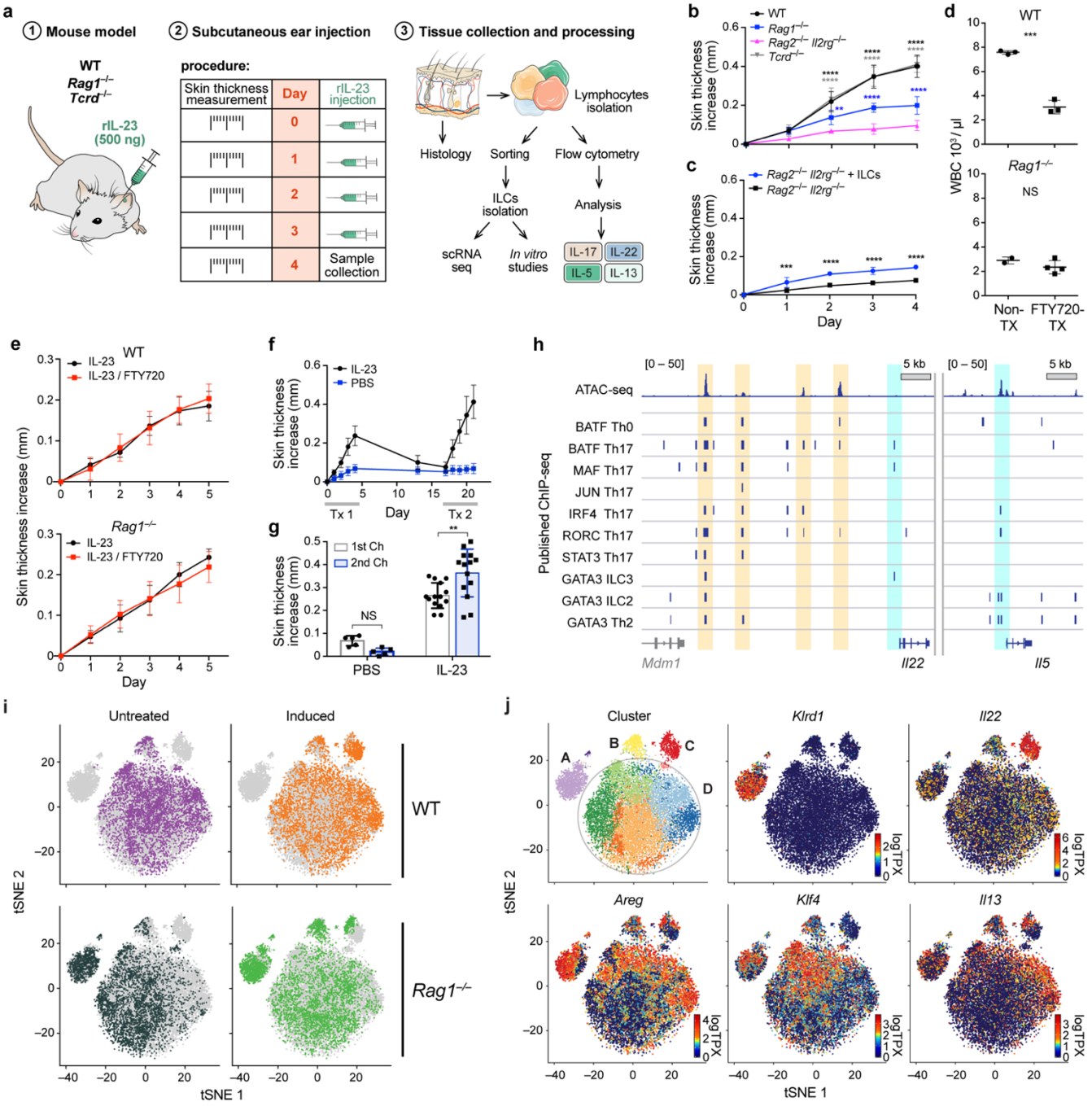
a
① Mouse model
② Subcutaneous ear injection
③ Tissue collection and processing
WT
Rag1−/−
Tcrd−/−
rIL-23
(500 ng)
procedure:
Skin thickness measurement
Day
rIL-23 injection
Sample collection
Lymphocytes isolation
Histology
Sorting
Flow cytometry
ILCs isolation
Analysis
scRNA seq
In vitro studies
IL-17
IL-22
IL-5
IL-13
b
WT
Rag1−/−
Rag2−/− Il2rg−/−
Tcrd−/−
Skin thickness increase (mm)
c
Rag2−/− Il2rg−/− + ILCs
Rag2−/− Il2rg−/−
Day
d
WT
Rag1−/−
WBC 10³/ µl
NS
Non-TX
FTY720-TX
e
WT
IL-23
IL-23 / FTY720
Rag1−/−
Skin thickness increase (mm)
Day
f
IL-23
PBS
Tx 1
Tx 2
g
1st Ch
2nd Ch
NS
PBS
IL-23
h
[0 – 50]
5 kb
ATAC-seq
Published ChIP-seq
BATF Th0
BATF Th17
MAF Th17
JUN Th17
IRF4 Th17
RORC Th17
STAT3 Th17
GATA3 ILC3
GATA3 ILC2
GATA3 Th2
Mdm1
Il22
Il5
i
Untreated
Induced
WT
Rag1−/−
tSNE 1
tSNE 2
j
Cluster
A
B
C
D
Klrd1
Il22
Areg
Klf4
Il13
logTPX
tSNE 1
tSNE 2

Figure 2. Topic modeling of skin ILCs highlights repressive, quiescent-like state and multiple, distinct states of activation combined in cells. (A) Topic model concept in the context of single cell expression. Topics (top) consist of genes (middle), with distinct weights (gradient, **Methods**) based on their importance in the topic. Cells (bottom), are scored based on the contribution of each topic (color) in them; a cell can thus have multiple topics. (**B–E),** Results of LDA on ILCs with 15 topics (**Methods**). (B,C) Topics reveal complex relationships among clusters. TSNE of cells colored if they are highly weighted for Topic 11 and gray otherwise, with color code reflecting cluster membership as in **Fig. 1J** (**B**, left), or by expression (color bar, logTPX (**Methods**)) of *Cd83*, a Topic-11 associated gene (**b,** right). Analogous plots for Topic 13 (**c,** left) and its associated gene *Srgn* (**C**, right). (D,E) Topics with high weights in cells from untreated (Topics 2, 8, and 11) *vs.* induced (Topics 4, 13, and 15) conditions. (**D**) For each topic shown are a bar plot of top scoring genes (y axis), ranked by a score (x axis, logarithmic scale) of how well the gene distinguishes this from other topics (**Methods**); a tSNE (as in **Fig. 1I**) with cells colored by the topic's weight in the cells (column j of the cell-by-topic weight matrix θ (θ_{*j}) for Topic j); and a graph of the empirical cumulative density function (y axis) of topic weights θ_{*j} (x axis) for cells grouped by treatment or genotype (as in **Fig. 1H**). (**E**) Examples of topic-associated genes. Gene expression (y axis, logTPX) as a smoothed function of the topic weight (log θ_{*j}, x axis), for each of the topics highlighted in **D** (color)

Figure 2

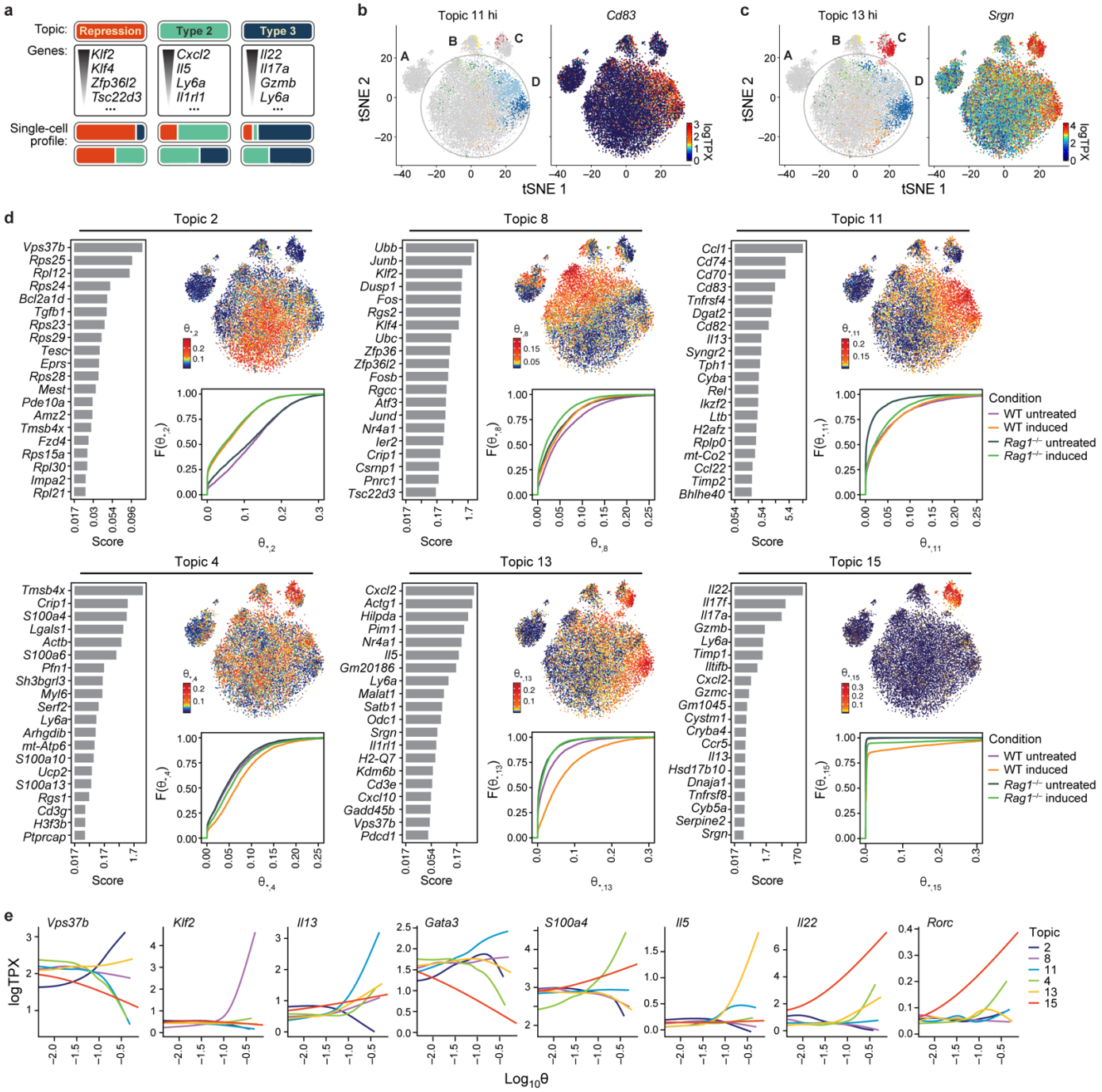
a
Topic:
Repression
Type 2
Type 3
Genes:
Klf2
Klf4
Zfp36l2
Tsc22d3
Cxcl2
Il5
Ly6a
Il1rl1
Il22
Il17a
Gzmb
Ly6a
Single-cell profile:
b
Topic 11 hi
Cd83
tSNE 2
tSNE 1
logTPX
c
Topic 13 hi
Srgn
d
Topic 2
Topic 8
Topic 11
Topic 4
Topic 13
Topic 15
Score
Condition
WT untreated
WT induced
Rag1−/− untreated
Rag1−/− induced
e
Vps37b
Klf2
Il13
Gata3
S100a4
Il5
Il22
Rorc
logTPX
Log10θ
Topic
2
8
11
4
13
15

Figure 3. Inference of an IL-23–induced dynamic trajectory from quiescent-like ILCs through classically activated ILC2s to pathological *Il13/Il17a/Il22*-expressing ILC3-like cells. (A,B) Distinct topics suggest a dense continuum of states undergoes a dynamic transition during psoriasis induction. Shown is a diffusion map constructed only from cells highly weighted for selected topics (Topics 2, 4, 8, 11, 13, or 15) and the corresponding topic-specific genes (**Methods**). Plots of DC2 (x axis), DC3 (y axis) and DC1 (z axis), show cells (dots) colored by either *in vivo* treatment and genotype (**A**) or by topic weight (log θ_{*j}, color bar) (**B**). Gray arrows (**A**) indicate an implicit direction of induction. **(C,D)** A naïve-induced trajectory across DC1 in a focused diffusion map from Topics 8, 13, and 15. DC 1 (x axis), DC2 (y axis), and DC3 (z axis) of a focused diffusion map, with cells colored as in **A** by *in vivo* treatment and genotype (**C**), or as in **B** by topic (**D**). **(E)**, Key genes associated with the trajectory from quiescent-like ILCs to activated ILC2s to ILC3-like cells. Expression (color scale, logTPX) of genes (rows) in cells (columns) associated with Topics 8 ("naïve-quiescent"), 13 ("*Il5*/*Cxcl2*"), and 15 ("*Il22/Il17a*"), with cells marked by *in vivo* condition and genotype (top bar; colored as in **A**). Grey scale bars: Topic weights for cells (log θ_{*j}) (horizontal bars) and genes (log $\beta_{j,*}$, where β is the topic-by-gene weight matrix; vertical bars) illustrate mixtures of functional states.

Figure 3

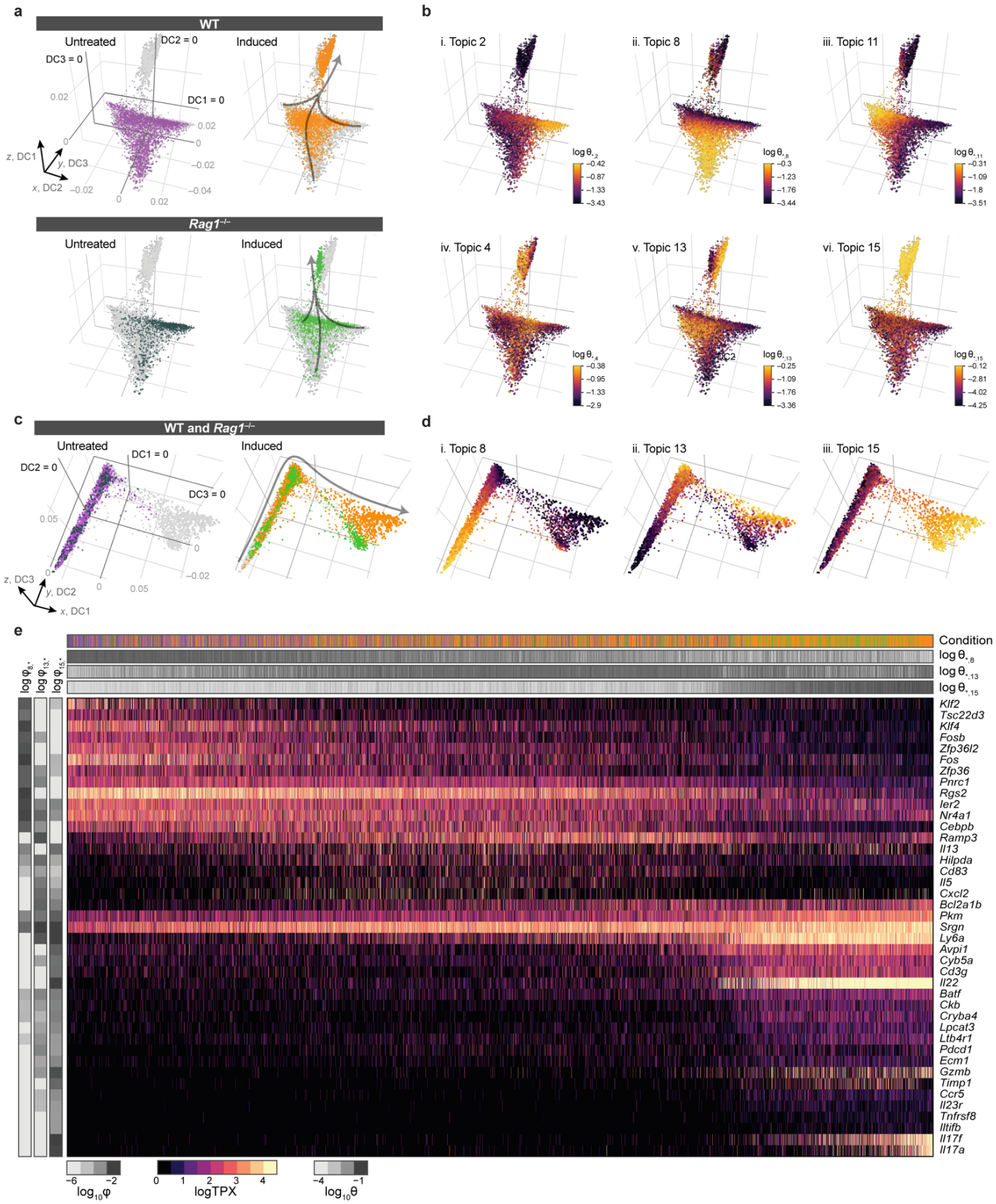
a
WT
Untreated
Induced
DC2 = 0
DC3 = 0
DC1 = 0
z, DC1
y, DC3
x, DC2
Rag1−/−
Untreated
Induced
b
i. Topic 2
ii. Topic 8
iii. Topic 11
iv. Topic 4
v. Topic 13
vi. Topic 15
c
WT and Rag1−/−
Untreated
Induced
DC2 = 0
DC1 = 0
DC3 = 0
z, DC3
y, DC2
x, DC1
d
i. Topic 8
ii. Topic 13
iii. Topic 15
e
Condition
log θ*,8
log θ*,13
log θ*,15
log φ8,*
log φ13,*
log φ15,*
Klf2
Tsc22d3
Klf4
Fosb
Zfp36l2
Fos
Zfp36
Pnrc1
Rgs2
Ier2
Nr4a1
Cebpb
Ramp3
Il13
Hilpda
Cd83
Il5
Cxcl2
Bcl2a1b
Pkm
Srgn
Ly6a
Avpi1
Cyb5a
Cd3g
Il22
Batf
Ckb
Cryba4
Lpcat3
Ltb4r1
Pdcd1
Ecm1
Gzmb
Timp1
Ccr5
Il23r
Tnfrsf8
Iltifb
Il17f
Il17a
log10φ
logTPX
log10θ

Figure 4. *In vivo* validation of the trajectory from quiescent-like ILCs in healthy skin to differentiation of ILC2s to ILC3-like cells during IL-23–induced response. (A) ATAC-seq confirms quiescent-like ILCs. Open chromatin peaks (light blue shaded boxes) of ATAC-Seq reads (blue tracks) from sorted skin ILCs from untreated mice at TSS of key genes (bottom track) responsible for quiescence and repression of type 3 programs. **(B-D)** ILC2-ILC3 plasticity revealed by IL-5 fate mapping and IL-22^{BFP} and IL-17A^{GFP} reporter mouse. (**B**) Fate mapping scheme. IL-5 Fate mouse reporter combined with IL-17A^{GFP} and IL-22^{BFP} reporters showing possible outcomes of skin ILC activation, in a scenario with ILC2 to ILC3 differentiation (top) *vs*. direct ILC3 differentiation (bottom). (**C**) IL-23 induction increases the number of IL-22– and IL-17A–producing cells, including among cells formerly producing IL-5 ("exIL-5"), especially after secondary challenge. Number of cells (y axis) with each reporter configuration (top label) in IL23-treated and PBS controls (x axis) in the first (circles) and second (squares) challenge. **(D)** exIL-5 cells that transdifferentiated to produce IL-22 and IL-17A do not produce IL-5 anymore. FACS plots of the expression of YFP (x axis) and IL22-BFP (x axis, top) or IL17A-GFP (x axis, bottom). (**E,F),** IL-23 treatment induces IL-13/IL-22 and IL-13/IL-17A double-producing populations and elevates IL-13/IL-22 double production in *Rag1* deficient mouse. (**E**) Levels of IL-13 (x axis) and IL-22 (y axis) measured by intracellular cytokine staining of skin ILCs in wild type (top), *Rag1*$^{-/-}$ (middle) and *Tcrd*$^{-/-}$ (bottom) mice. (**F**) Mean number of cells (y axis) among single producers and co-producers in each mouse genotype (x axis). Error bars, SD; *p<0.0332, **p<0.021, ***p<0.0002, ****p<0.0001 by two-way ANOVA.

Figure 4

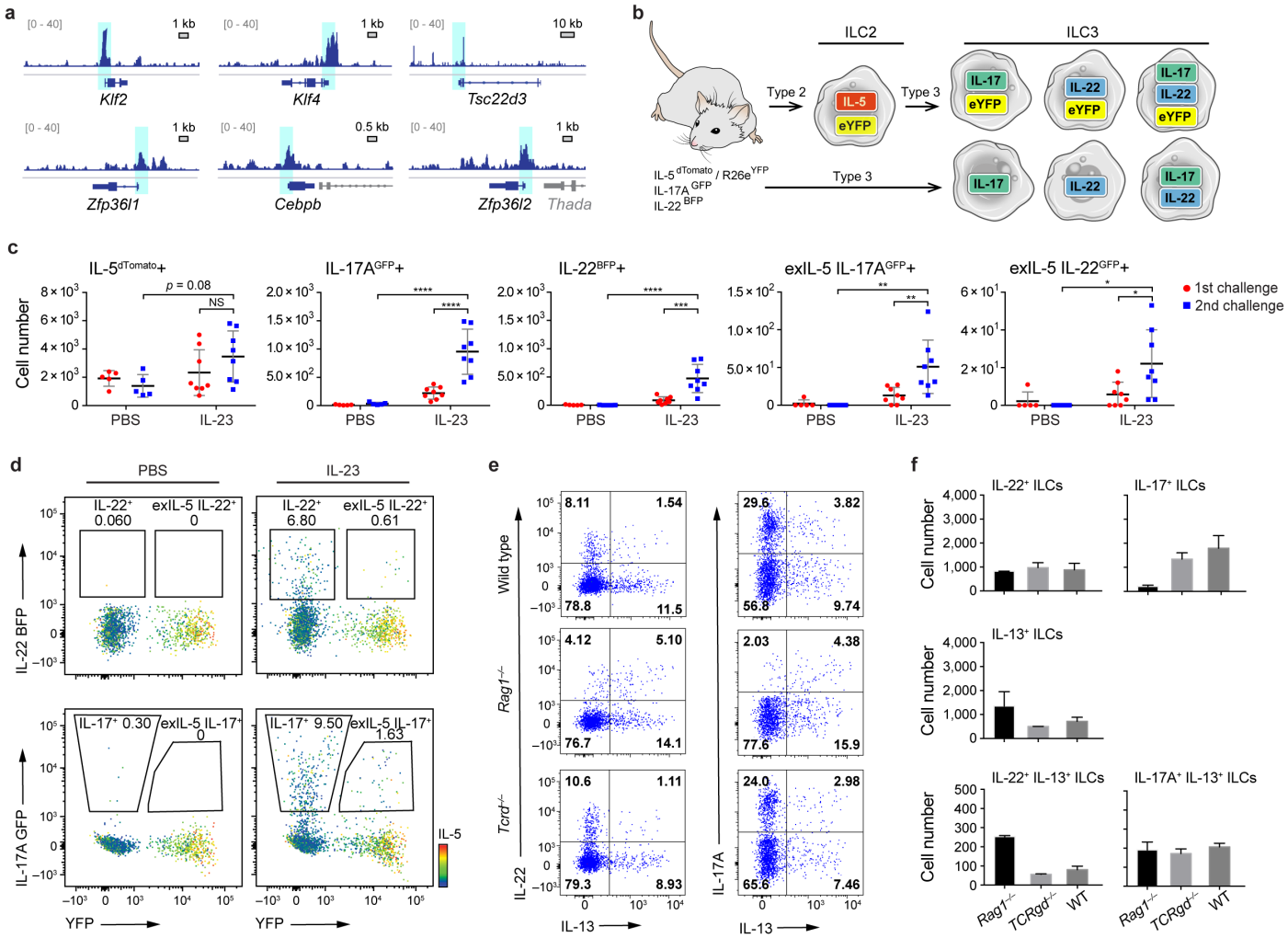
a
[0 - 40]
1 kb
Klf2
Klf4
10 kb
Tsc22d3
0.5 kb
Zfp36l1
Cebpb
Zfp36l2
Thada
b
ILC2
ILC3
Type 2
Type 3
IL-5
eYFP
IL-17
IL-22
IL-5 dTomato / R26e YFP
IL-17A GFP
IL-22 BFP
c
IL-5dTomato+
IL-17AGFP+
IL-22BFP+
exIL-5 IL-17AGFP+
exIL-5 IL-22GFP+
Cell number
p = 0.08
NS
PBS
IL-23
1st challenge
2nd challenge
d
IL-22+ 0.060
exIL-5 IL-22+ 0
IL-22+ 6.80
exIL-5 IL-22+ 0.61
IL-17+ 0.30
exIL-5 IL-17+ 0
IL-17+ 9.50
exIL-5 IL-17+ 1.63
IL-22 BFP
IL-17A GFP
YFP
IL-5
e
Wild type
Rag1−/−
Tcrd−/−
IL-22
IL-17A
IL-13
8.11
1.54
78.8
11.5
29.6
3.82
56.8
9.74
4.12
5.10
76.7
14.1
2.03
4.38
77.6
15.9
10.6
1.11
79.3
8.93
24.0
2.98
65.6
7.46
f
IL-22+ ILCs
IL-17+ ILCs
IL-13+ ILCs
IL-22+ IL-13+ ILCs
IL-17A+ IL-13+ ILCs
Cell number
Rag1−/−
TCRgd−/−
WT

Figure S1. Characterization of skin immune cells to IL-23 induction, Related to Figure 1

(A) Increase in ear skin thickness is significantly higher in response to IL-23 treatment than PBS vehicle and is dependent on *Rorc*. Increase in ear thickness (y axis, mm) following treatment with IL-23 (blue) or PBS vehicle (black) in WT (top) or *Rorc*$^{-/-}$ (bottom) mice.

(B and C) Immune cell composition and skin phenotype in different mouse genotypes. (B) Top: Number of cells (y axis) producing IL-22 or IL-17 (x axis) among ILCs (black bars), αβT cells (grey bars) and γδ T cells (white bars) in WT, *Tcrd*$^{-/-}$ (lack γδ T cells), *Rag1*$^{-/-}$ (lack all T and B cells), and *Rag2*$^{-/-}$ *Il2rg*$^{-/-}$ mice (also lack ILCs) mice. Bottom: Number of total CD45^{+} (left, y axis) or total ILCs (right, y axis) in WT, *Tcrd*$^{-/-}$, *Rag1*$^{-/-}$, and *Rag2*$^{-/-}$ *Il2rg*$^{-/-}$ mice (x axis). (C) H&E stains of ear sections in each genotype except *Rag2*$^{-/-}$ *Il2rg*$^{-/-}$ mice. Arrows: Acanthosis.

(D) Expression of type 2 and type 3 related genes in cultured naïve skin ILCs. Shown are relative expression levels (y axis, by qPCR) in ILCs cultured with different cytokines (x axis, table at bottom).

(E) FTY720 treatment does not impact increased susceptibility to a secondary challenge with IL-23. Skin thickness (y axis, 0.1mm) over time (x axis, days) in mice following treatment with either IL-23 or IL-23 and FTY720. Bottom bars: period of primary (left bar) and secondary (right bar) challenge.

(F and G) ATAC-seq of sorted skin ILCs from untreated mice. Mapped ATAC-seq reads from sorted skin ILCs from untreated mice (top tracks) at different loci (bottom tracks) of interest. Blue shaded areas: TSS; Beige shared areas: open chromatin peaks at key TF binding sites, previously identified in CD4^{+} T cell ChIP-seq data (middle tracks). (F) Open chromatin peaks at TSS of *Gata3* (associated with mature ILC2) but not *Rorc* (ILC3) and *Tbx21* (ILC1). (G) Open chromatin peaks at TF binding sites in the *Il17a and Il17f* promoter (beige), and at the TSS of *Il13* but not *Il17a,Il17f* (blue).

(H), Cluster B reflects cycling ILCs. tSNE of 27,998 single ILC profiles (dots) colored by expression level (logTPX, color bar) of *Stmn1*.

Figure S1

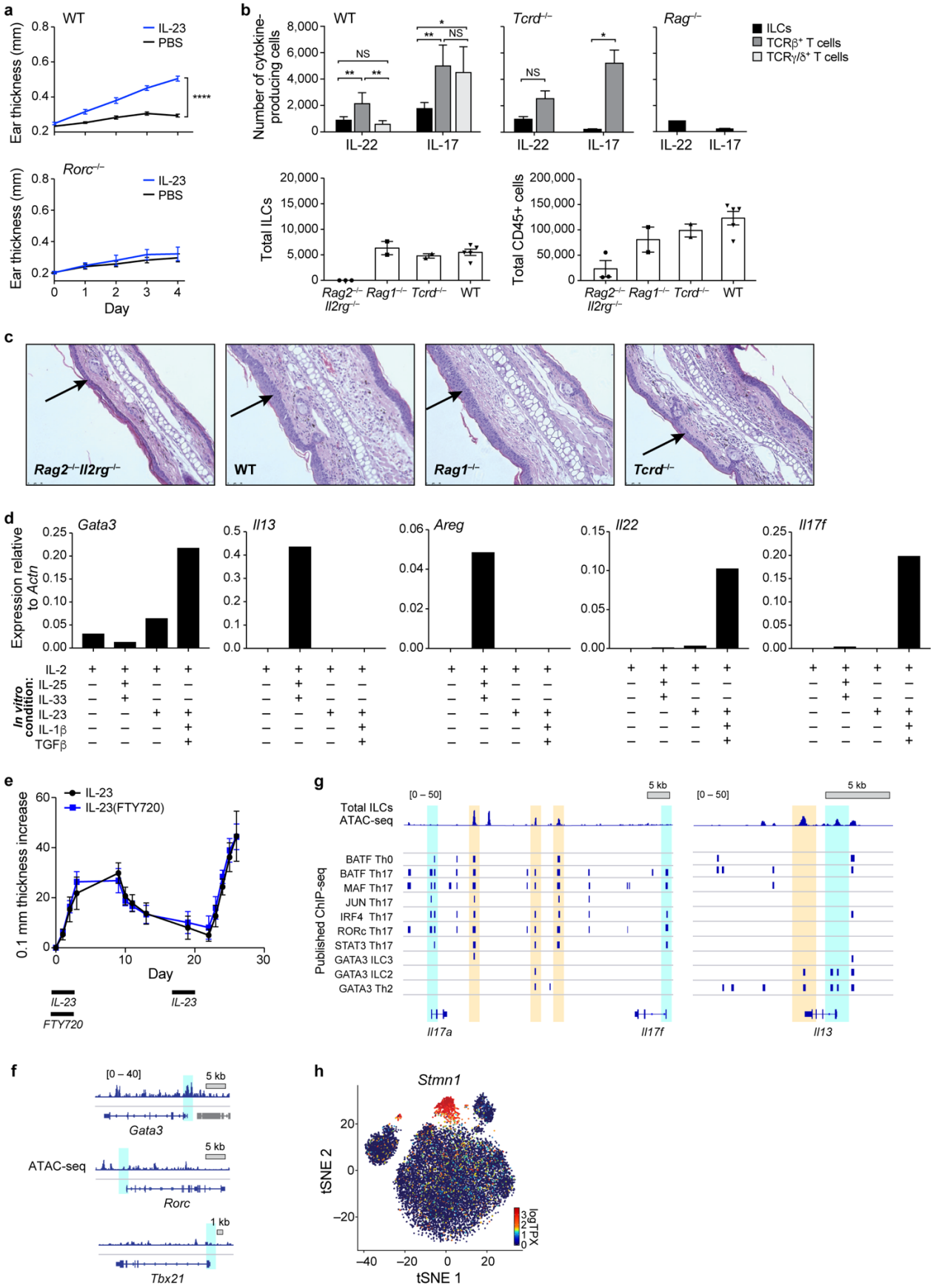
a
WT
IL-23
PBS
Ear thickness (mm)
****
Rorc−/−
Day
b
Number of cytokine-producing cells
NS
**
*
Tcrd−/−
Rag−/−
ILCs
TCRβ+ T cells
TCRγ/δ+ T cells
IL-22
IL-17
Total ILCs
Total CD45+ cells
Rag2−/− Il2rg−/−
Rag1−/−
WT
c
Rag2−/−Il2rg−/−
Rag1−/−
Tcrd−/−
d
Gata3
Il13
Areg
Il22
Il17f
Expression relative to Actn
In vitro condition:
IL-2
IL-25
IL-33
IL-23
IL-1β
TGFβ
e
IL-23
IL-23(FTY720)
0.1 mm thickness increase
Day
IL-23
FTY720
g
Total ILCs ATAC-seq
Published ChIP-seq
BATF Th0
BATF Th17
MAF Th17
JUN Th17
IRF4 Th17
RORc Th17
STAT3 Th17
GATA3 ILC3
GATA3 ILC2
GATA3 Th2
5 kb
Il17a
Il17f
Il13
f
Gata3
ATAC-seq
Rorc
Tbx21
1 kb
h
Stmn1
tSNE 1
tSNE 2
logTPX

Figure S2. Topic modeling also distinguishes cluster-specific, cell size, and cell quality related topics, Related to Figure 2.

(A) Selecting the number of topics. Akaike Information Criterion (AIC, red) and Bayesian Information Criterion (BIC, blue) value (y axis) for a range of the number K of topics. K=15 (dotted line) is at a point where the AIC curve decreases less steeply and the BIC curve begins to rise.

(B and C) Expression of example genes associated with key topics. (B) tSNE of 27,998 single ILC profiles (dots) colored by expression level (color bar, logTPX (**Methods**)) for genes in Topics 2, 4, 8, 11, 13, and 15.

(C) Gene expression (y axis, logTPX) as a function of the topic weight (log $\theta_{*,j}$, x axis), for each of these topics (color), for repressive gene *Zfp36l2* and activation-associated gene *Ly6a*.

(D) Summary of remaining topics not included in Fig. 2c. For each topic shown are a bar plot of top scoring genes (y axis), ranked by a score (x axis, logarithmic scale) of how well the gene distinguishes this from other topics (**Methods**); a tSNE (as in B) with cells colored by the topic's weight in the cells (column j of the cell-by-topic weight matrix θ ($\theta_{*,j}$) for Topic j); and a graph of the empirical cumulative density function (y axis) of topic weights $\theta_{*,j}$ (x axis) for cells grouped by treatment or genotype (as in Fig. 2c).

Figure S2

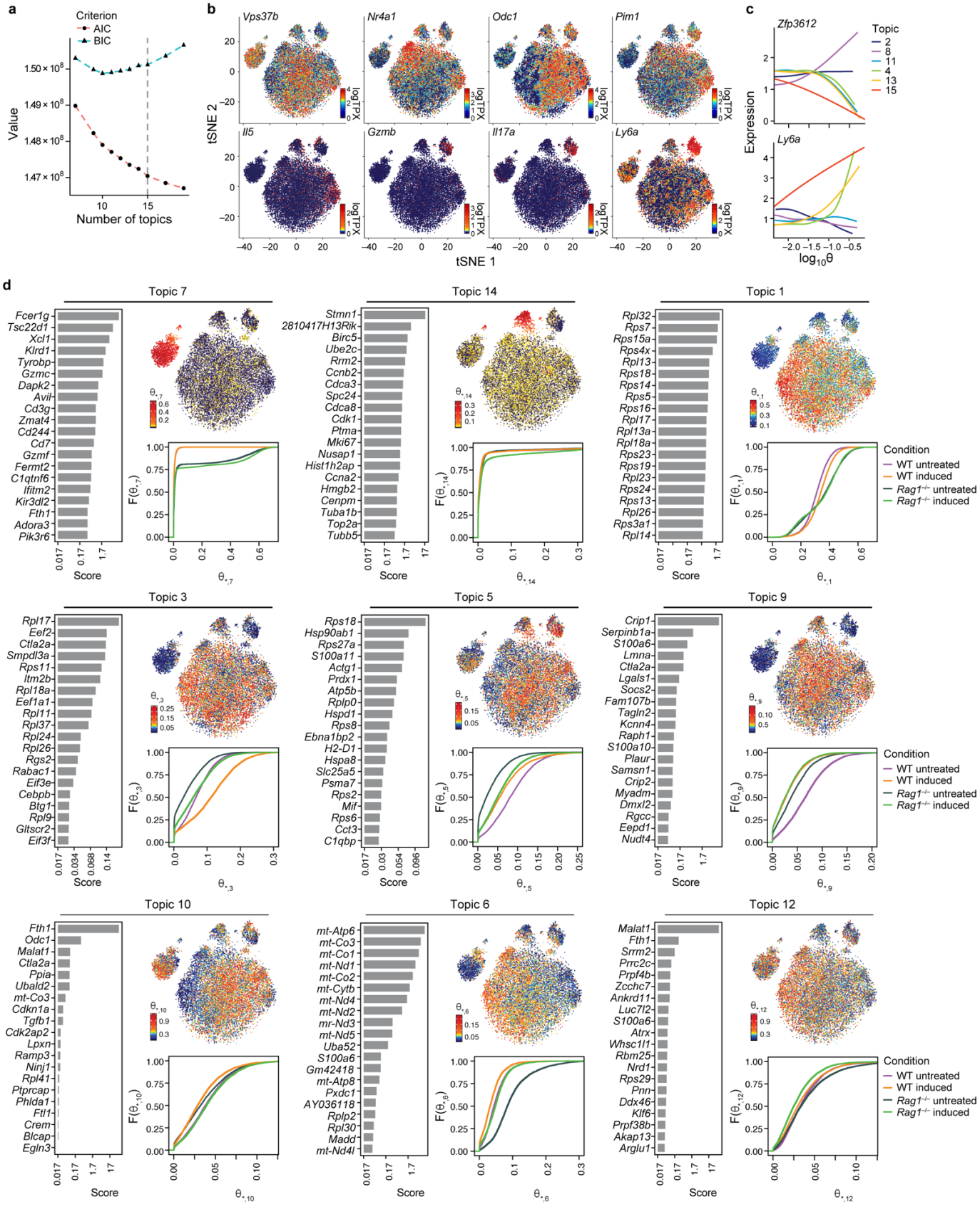
a
Criterion
AIC
BIC
Value
Number of topics
b
Vps37b
Nr4a1
Odc1
Pim1
Il5
Gzmb
Il17a
Ly6a
tSNE 2
tSNE 1
logTPX
c
Zfp3612
Ly6a
Topic
Expression
log10θ
d
Topic 7
Topic 14
Topic 1
Topic 3
Topic 5
Topic 9
Topic 10
Topic 6
Topic 12
Score
Condition
WT untreated
WT induced
Rag1-/- untreated
Rag1-/- induced

Figure S3. Diffusion map analysis based on topic model highlights an IL-23–induced dynamic trajectory, Related to Figure 3.

(A-C) Cell selection for diffusion map in Fig 3A and B. (A) Chosen topic weight thresholds. Empirical cumulative density function (y axis) of topic weights $\theta_{*,j}$ (x axis) of cells grouped and colored by *in vivo* treatment and genotype. Dotted line: topic weight threshold. (B and C) Cells with high weights in at least one key topic are chosen for the diffusion map. tSNE of 27,998 single ILC profiles (dots), with cells colored if they are weighted above the corresponding topic threshold from A (B, red) and chosen for the diffusion map (C, black), if they are highly weighted for Topics 2, 8, 11, 4, 13, or 15, but not for Topics 6 or 7.

(D and E) Topics 8, 13, and 15 highlight a potential naïve-induced trajectory across DC1. Plots of DC1 (x axis), DC3 (y axis), and DC4 (z axis) show cells (dots) colored by either *in vivo* treatment and genotype (D) or by topic weight (log $\theta_{*,j}$, color bar) (E). Gray arrows (D) indicate an implicit direction of induction.

Figure S3

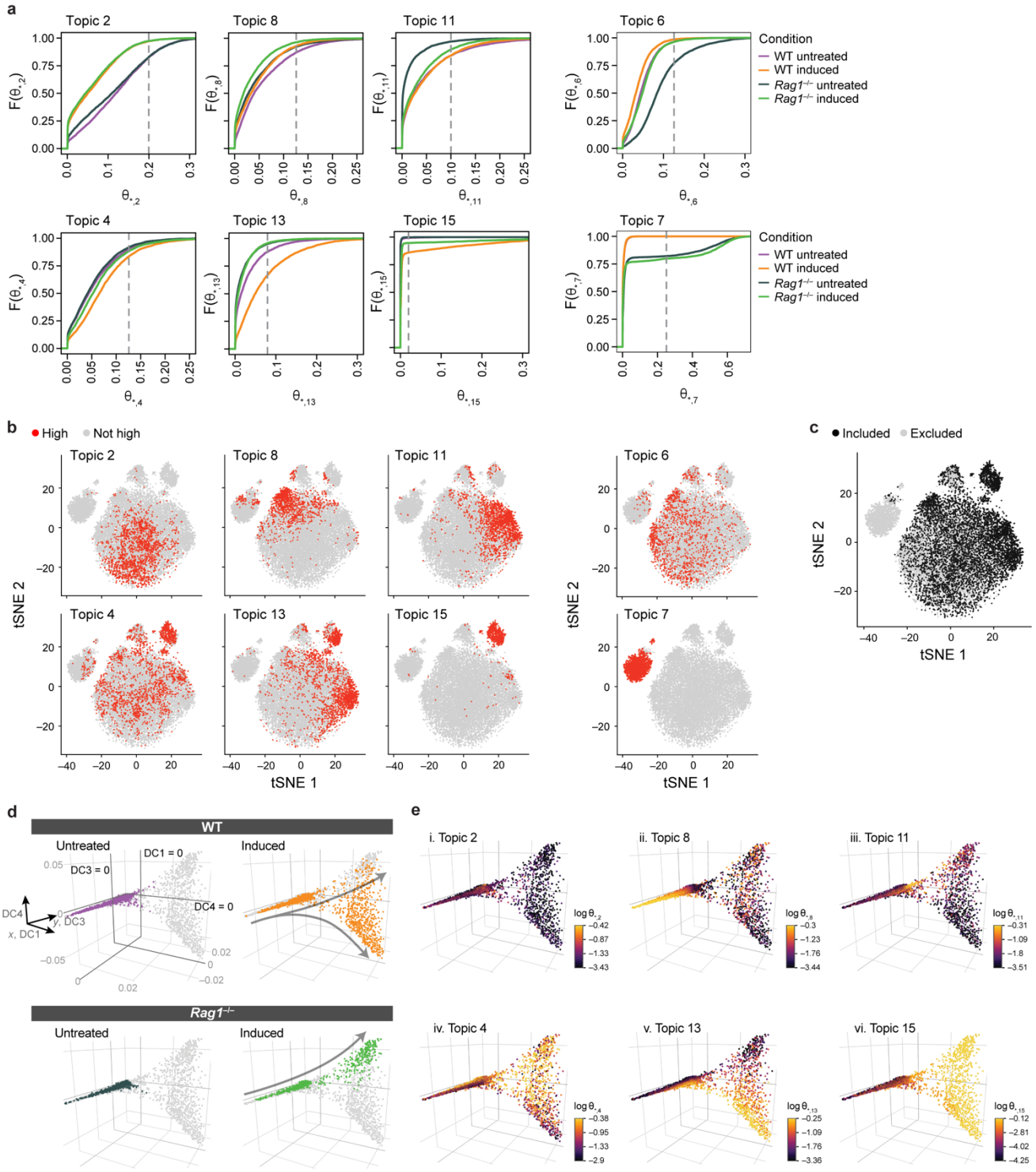
a
Topic 2
Topic 8
Topic 11
Topic 6
Topic 4
Topic 13
Topic 15
Topic 7
Condition
WT untreated
WT induced
Rag1−/− untreated
Rag1−/− induced
b
High
Not high
tSNE 1
tSNE 2
c
Included
Excluded
d
WT
Untreated
Induced
DC1 = 0
DC3 = 0
DC4 = 0
z, DC4
y, DC3
x, DC1
Rag1−/−
e
i. Topic 2
ii. Topic 8
iii. Topic 11
iv. Topic 4
v. Topic 13
vi. Topic 15

Figure S4. Computational and experimental quality control and data processing.

(A) IL-23 skin injection model in *Il5*^{dTomatoCre} (Red5) mouse strain. Increase in skin thickness (mm, y axis) over time (days, x axis) in homozygote Red5/Red5 mouse strain lacking expression of IL-5 cytokine (black) and Red5/+ mouse (blue) shown little difference.

(B and C) Quality control and filters in scRNA-Seq. (B) Minimum and maximum thresholds (red) of log UMI counts (x axis) and log gene counts (y axis) for each condition. Cells (dots) that were filtered out are marked in red. (C) Left: Histogram of the % of mitochondrial genes detected across all cells. Right: Box plot of the % of mitochondrial genes of all detected genes in each sample type. Dashed lines: thresholds.

(D) Distributions for the number of UMI counts in each sample, used to compute logTPX (**Methods**).

(E) Variable gene selection. For each sample (panel) shown are the coefficient of variation (CV, y axis) as a function of mean counts (x axis) for each gene (dot). Black curve: null model (**Methods**). Blue: genes with sufficiently greater CV than in the null model, which are retained as variable genes.

Figure S4

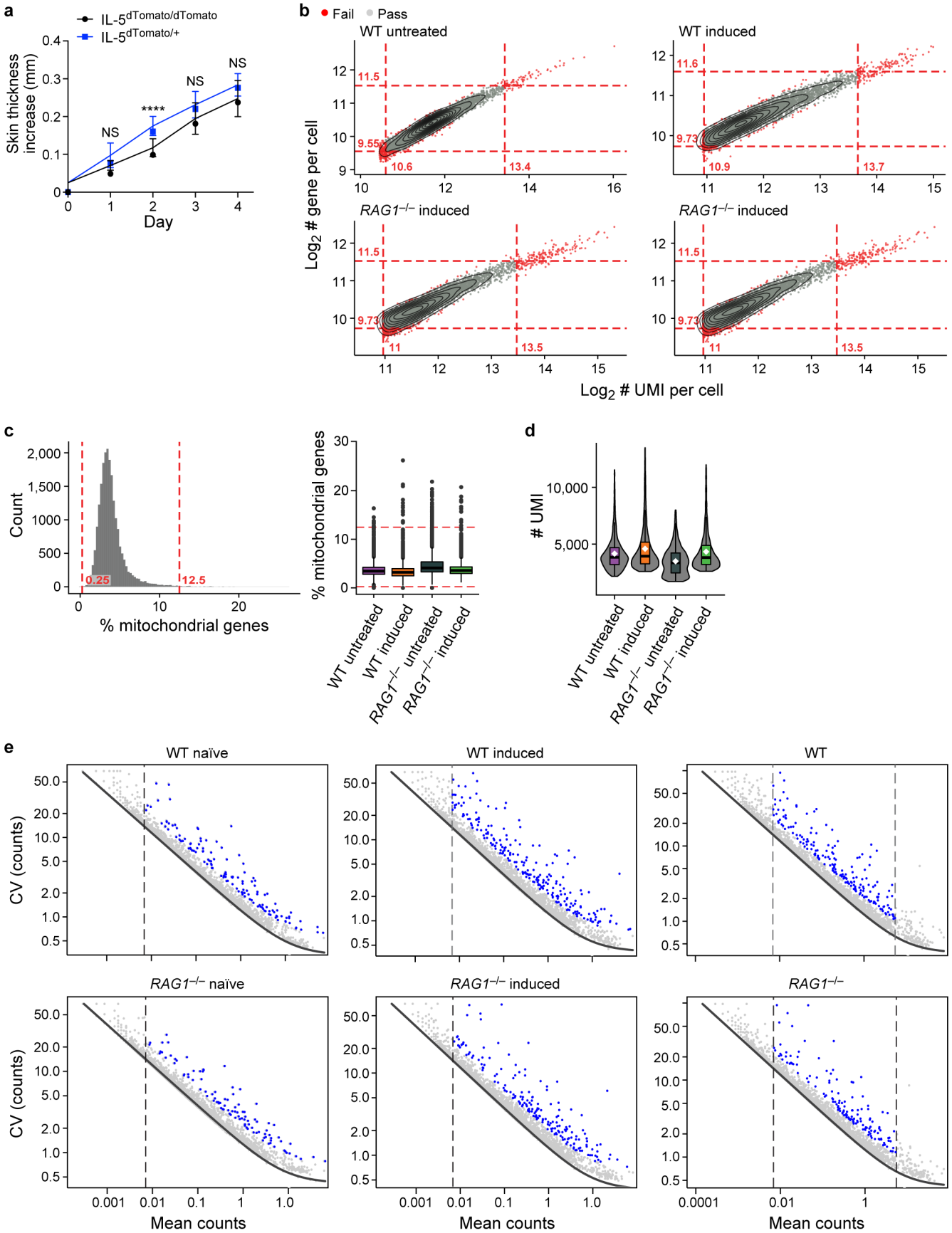
a
IL-5dTomato/dTomato
IL-5dTomato/+
Skin thickness increase (mm)
Day
NS
****
NS
NS
b
Fail
Pass
WT untreated
WT induced
RAG1−/− induced
RAG1−/− induced
Log2 # gene per cell
Log2 # UMI per cell
c
Count
% mitochondrial genes
0.25
12.5
% mitochondrial genes
WT untreated
WT induced
RAG1−/− untreated
RAG1−/− induced
d
UMI
WT untreated
WT induced
RAG1−/− untreated
RAG1−/− induced
e
WT naïve
WT induced
WT
RAG1−/− naïve
RAG1−/− induced
RAG1−/−
CV (counts)
Mean counts